Novel *KCNJ10* mutation identified in a SeSAME family compromise channel function and impairs *Drosophila* locomotor behavior

Ravi K Nadella[1], Anirudh Chellappa[1], Anand G Subramaniam[1], Aman Aggarwal[6,7], Ravi Prabhakar More[6], Mahalakshmi Dhana sekar[1], Srividya Shetty[1], Suriya Prakash[1], Nikhil Ratna[1], Vandana VP [5], Meera Purushottam[1], Jitender Saini[4], Biju Viswanath[1], PS Bindu[2], Madhu Nagappa[2], Bhupesh Mehta[3], Sanjeev Jain[1,6], Ramakrishnan Kannan[1#]

[#] Corresponding author

Affiliations

[1]Department of Psychiatry; [2]Department of Neurology; [3]Department of Biophysics; [4]Department of Neuroimaging and Interventional radiology; [5]Department of Speech Pathology and Audiology at National Institute of Mental Health and Neurosciences, Bangalore, India.

[6]National Centre for Biological Sciences, Tata Institute for Fundamental Research, Bangalore, India

[7]Manipal Academy of Higher Education, Manipal, Karnataka, India

Address for correspondence

Ramakrishnan Kannan, PhD
National Institute of Mental Health and Neurosciences (NIMHANS), Bengaluru, Karnataka, India PIN: 560029
Phone: 091-80-26995791
Fax:+91-80-26564830
Email: kannan@nimhans.edu.in
ORCID #: 0000-0001-7717-0516

Keywords

SeSAME syndrome, Kir4.1, Runs of homozygosity, *Drosophila* behavior

Abstract

Deficits in the inwardly rectifying K^+ channel, Kir4.1, cause SeSAME syndrome, autism spectrum disorders with seizures, multiple sclerosis, Huntington's disease and Rett syndrome. Understanding how deficits in a single gene can accomplish such diverse neurological symptoms, requires that we know the functional role of Kir4.1 in the nervous system. We used whole exome sequencing (WES), channel physiology in patient-specific lymphoblastoid cells (LCLs) and established a *Drosophila* model to examine the functional effects of a *KCNJ10* variant identified in SeSAME-like family. WES analysis of six related affected individuals, born out of consanguineous parentage, identified $KCNJ10^{T290A}$ variant residing within a long homozygous stretch in Chr1. The membrane potential of LCLs carrying $KCNJ10^{T290A}$ variant were significantly depolarized and exhibit defects in potassium permeability, thus demonstrating a loss-of-function effect. *Drosophila irk2 mutant*, a human homolog of Kir4.1, exhibited impairment locomotion, shortened life-span and age-dependent degeneration of dopaminergic neurons in the adult brain. Finally, neural specific expression of either Kir4.1 or Irk2 alleviate *irk2* mutant phenotypes, while the $Kir4.1^{T290A}$ and $Irk2^{T290A}$ mutant proteins failed to do so. These results imply the functional conservation of Kir4.1 across species thereby elevate the potential of using *Drosophila* model to improve our understanding of the SeSAME syndrome. Our results emphasize the importance of Kir4.1 in regulating extracellular K^+ homeostasis, which is central to patterning of nervous system during development.

Introduction

SeSAME syndrome (OMIM#612780), characterized by Seizures, Sensorineural deafness, Ataxia, Mental retardation and Electrolyte imbalance is a rare, autosomal recessive and multisystemic disorder. Otherwise known as EAST (Epilepsy, Ataxia, Sensorineural deafness, Tubulopathy) syndrome, SeSAME is predominantly caused by homozygous or compound heterozygous mutations in *KCNJ10* gene (Bockenhauer et al., 2009; Scholl et al., 2009) encoding Kir4.1, an inwardly rectifying potassium channel with diverse expression patterns in multiple cell types of central and peripheral nervous system (Reichold et al., 2010; Hibino et al., 2010; Paulais et al., 2011; Thompson et al., 2011; Kelley et al., 2018; Larson et al., 2018; Song et al., 2018). Depending on tissue localization and assembly of Kir4.1 subunit, which can constitute homotetramers and/or heterotetramers with Kir5.1 (*KCNJ16*), these channels exhibit distinctive physiological properties (Paulais et al., 2011; Pessia et al., 2001). Kir4.1 channel play conspicuous roles in the maintenance of resting membrane potential (Kofuji et al., 2000), facilitation of glutamate uptake (Djukic et al., 2007), potassium siphoning by glial cells (Neusch et al., 2006; Song et al., 2018), cell volume and peak strength regulation of fast α-motor neurons (FαMNs; Kelley et al., 2018), axonal integrity through myelination by oligodendrocytes (Neusch et al., 2001; Schirmer et al., 2018; Larson et al., 2018) and cell migration (dehart et al., 2008). Dysfunction of Kir4.1 has been associated with a spectrum of neurodegenerative conditions like idiopathic epilepsy (Buono et al., 2004; Heuser et al., 2010; Lenzen et al., 2005), autism spectrum disorder with seizures (Sicca et al., 2011; Sicca et al., 2016; Larson et al., 2018), Huntington's disease (Tong et al., 2014), multiple sclerosis (Srivatsava et al., 2012; Brickshawana et al., 2014; Nwaobi et al., 2016; Gu et al., 2016) and Rett syndrome (Olsen et al., 2015; Kahanovitch et al., 2018).

Given the genetic redundancy and compensation effects of mammalian Kir channel proteins, invertebrate *Drosophila* model system offers an excellent choice to investigate the physiological

functions of Kir mutant proteins. The *Drosophila* genome encodes only three Kir channel proteins; Irk1 (Kir2 family), Irk2 (Kir4 and Kir5 family) and Irk3 (Kir1 family) and are shown to be critical for patterning of nervous system during development (Chen and Swale, 2018). In contrast, fifteen Kir channels have been identified in mammals which are grouped into seven families based on sequence similarity and functional properties (Hibino et al., 2010). Several Kir channels (Kir2.1, Kir3, Kir4 and Kir6) that are primarily expressed in thalamus, cortex, brainstem and hippocampus are associated with epilepsy (Higashi et al., 2001; Villa and Combi, 2016). Kir channels display greater inward K^+ flow at negative resting membrane potential to equilibrium potential for K^+ (*E*k), while at more positive membrane potentials, outward flow of K^+ is inhibited by intracellular Mg^{2+} and polyamines (Lopatin et al., 1994). Overall Kir channel allows K^+ ions to pass easily inward than outward direction.

We identified a novel homozygous mutation in *KCNJ10* by WES of all six affected members of a family diagnosed with SeSAME syndrome. Next, using a series of whole-cell patch clamp experiments in patient-specific LCLs, we found that the variant compromised the membrane physiology of Kir4.1. Furthermore, to investigate its role in the *Drosophila* nervous system, we isolated and characterized *irk2* mutant alleles. *irk2* mutants exhibited shortened-life span, stereotyped locomotor patterns and age-dependent degeneration of dopaminergic neurons in the adult brain, which are in part, analogous to the neurological phenotypes observed in SeSAME syndrome. Finally, we found that the neural specific overexpression of mutant proteins; neither Irk2 nor Kir4.1 failed to alleviate *irk2* whole mutant phenotypes unlike the wild type proteins demonstrating the loss-of-function of mutant Kir4.1^{T290A}. These findings emphasize the crucial physiological role of Kir4.1 from invertebrates to mammals.

Materials and Methods

Patient recruitment, genomic DNA isolation and generation of lymphoblastoid cells

The subjects were identified through the clinical services of NIMHANS. Various members of the family had been identified over many years, and the clinical information was collated. In addition, other branches of the family were identified and invited to participate in the study. The study protocol was approved by Institutional Human Ethics Committee and Institutional Stem Cell committee at National Institute of Mental Health and Neurosciences (NIMHANS), Bangalore, India. Patients were referred for biochemical evaluation and selected for further analysis by presence of seizures, ataxia, mental retardation, hearing impairment. Five ml of venous blood was collected in EDTA treated tubes (Becton-Dickinson) using standard procedures and genomic DNA was isolated using NucleoSpin® Blood L (Macherey-Nagel GmbH & Co. KG) for whole exome sequencing (WES). In addition, six ml of venous blood was collected separately in sodium heparin tubes (Becton-Dickinson) for isolation of peripheral blood mononuclear cells (PBMC) using SepMate™ tubes (STEMCELL Technologies) and histopaque-1077 (Sigma Aldrich) as a density gradient. For generation of lymphoblastoid cells (LCLs), PBMCs were transformed by Epstein Barr virus (EBV) using a standard protocol (Hui-Yuen et al., 2011). All six LCLs suspensions were cultured in RPMI 1640 medium pH 7.4 supplemented with 10% fetal bovine serum (FBS), 4 mM glutamine and streptomycin/penicillin antibiotic cocktail. Cells were maintained in a humified atmosphere of 5% CO_2, 95% air at 37^{o}C, the medium was replaced every 3rd day and cells were passaged once a week. Stabilized LCLs were further karyotyped using the G-banding approach (Bradley Howe et al., 2014), STR profiling

[GenePrint® 10 System (Promega)] using blood and LCL DNA was done to confirm sample identity.

Whole exome sequencing, variant calling, quality check and annotation

The blood DNA was extracted for 10 samples [unaffected parents, (n=4), and affected offsprings, (n=6)], and the library was prepared using Nextera Rapid Capture and Expanded Exome Kits. The library was further subjected to WES, performed on Illumina Hi-Sequencer to generate pair-end reads (150bp*2). We followed whole exome sequence analysis pipeline used by Suhas et al., 2018. FastQC (v0.11.5) (http://www.bioinformatics.babraham.ac.uk/projects/fastqc) was used for the quality of raw reads, which examine per base and per sequence quality scores, per base and per sequence GC content, per base N content and sequence length distribution. Prinseq-lite-0.20.4 tool was used to trim poor quality region (http://prinseq.sourceforge.net/) and adapterremoval-2.1.7 (Schubert et al., 2016) was used to remove adapter contamination in raw reads. Filtered reads with a quality score (Q)>20 were aligned to the human reference genome hg19 (GRCh37) using BWA (v0.5.9) (Li and Durbin, 2009). SAM to BAM conversion and sorting were done with Samtools 1.3 tool (https://sourceforge.net/projects/samtools/files/samtools/1.3/). Then the PCR duplicates were removed using PICARD tools (v1.96) (https://broadinstitute.github.io/picard/) and the INDELS were realigned using GATK (v3.6) (McKenna et al., 2010). The BAM alignment was subjected to QC using Qualimap (v2.2) (Okonechnikov et al., 2016). VarScan (v2.3.9) (Coverage=8, MAF>=0.25, *p*-value<0.001) was used to call for SNPs and INDELS (Koboldt et al., 2013). The quality of VCF file was checked using RTG tools 3.7.1 (https://github.com/RealTimeGenomics/rtg-tools/releases). All samples annotation was performed using ANNOVAR tool (Wang et al., 2010). Population controls (n=7) representing three religious groups (Group A, B, and C) matched for age, sex and ethnicity, were obtained from INDEX-db (Ahmed et al., 2018). All controls passed the age of risk i.e., 45 years, for neuropsychiatric illnesses, except for the outbred Parsi (religious group 3) individual (age=26), who was included as an outlier. All the controls were of southern Indian ethnic origin except for the Parsi. To validate *KCNJ10* variant identified by whole exome sequencing, we performed Sanger validation using the following gene specific primers: Forward (CATTCGTTTCAGCCAGCATGC) and Reverse (TCAGACATTGCTGATGCGCA).

Assessing runs of homozygosity (ROH)

Exome-wide F-statistics was calculated using the --het option in *vcftools* (v0.1.5), for every sample, to investigate whether levels of heterozygosity differed between the affected siblings, unaffected parents and population controls (Danecek et al., 2011). Runs of homozygosity (ROH) was detected in all samples using --homozyg option in PLINK (v1.9) (Purcell et al., 2007). The minimum length for a tract to qualify as ROH was set to 500kb and the minimum number of variants constituting an ROH was set to 100. A maximum of 3 intervening heterozygous variants were allowed within a ROH window. ROH density was set to default i.e., an ROH must have at least one variant per 50kb, on an average. The centromeric, X, Y and mitochondrial variants were ignored during this analysis. The stretches that were shared between all the affected individuals but not observed in either of the parents or the population controls were thus notified as $ROH_{affected}$, which were identified by using a combination of *intersect* and *subtract* functions in *bedtools* (v2.22) (Quinlan and Hall, 2010). The variants were annotated using variant effect predictor (VEP GRCh37) (McLaren et al., 2016).

Experiments with lymphoblastoid cells

Whole-cell patch clamp electrophysiology

For all electrophysiology experiments, the following LCLs were used. One healthy wild type control (not related to the family), two unaffected parental controls (III.11 and III.12) and four affected individuals (IV.2, IV.3, IV.4, IV.5) from SeSAME-like family described in this study. Cells in suspension are resuspended in fresh RPMI culture media and dissociated to achieve at least 40% of single cells in suspension. Thereafter the cells were plated in 15mm diameter cover slips (acid-treated, ethanol washed and air dried) coated with poly-$_D$-lysine (A-003-M EMD Millipore). Cells were kept in culture incubator (conditions as described above) for half hour before recordings. After establishment of whole-cell configuration, we immediately measured the membrane potential (*Vm*) of LCLs. A pulse protocol was applied in which *Vm* held at resting membrane potential and then stepped to test potentials between -120 to 40mV in 10mV steps for 140ms. To measure membrane currents (*nA*) we used a single electrode whole-cell patch clamp technique. For intracellular voltage-clamp recordings and positioning of perfusion micropipette, we used two Narishige hydraulic micomanipulators (MNW-203, Narashige Japan). Perfusion pipette with a tip diameter of 30-50 um was positioned close to the tip of patch pipette to facilitate rapid application of test solutions especially for experiments with increase in extracellular concentration of potassium. Electrodes for whole-cell patch experiments were pulled from borosilicate glass capillaries (IB150F-3, World Precision Instruments, USA) with resistance of 4-6megaohms in two step protocol using Sutter P-97 puller (Sutter Instruments Corp., Novato, CA). Micropipettes were filled with intracellular solution containing 120mM potassium D-gluconate (G4500, Sigma), 1mM $MgCl_2$, 15mM KCl, 1mM $CaCl_2$, 10mM EGTA, 10mM HEPES with 7.2 pH adjusted with KOH/HCl. After obtaining whole-cell mode, access resistance was 10-15megaohms. The extracellular recording solution contained 130mM $NaCl_2$, 3mM $CaCl_2$, 2.5mM $MgCl_2$, 15mM HEPES with 7.4 pH adjusted with NaOH. In experiments, where LCLs were puffed with high extracellular K^+, KCl was varied from 5-20 mM while NaCl was decreased to 110mM to adjust osmolarity. Recordings in LCLs, were performed using an HEKA triple patch clamp amplifiers (EPC 10 USB) at RT. To determine specificity of Kir4.1 current, we used 110µm/l $BaCl_2$ and to block endogenous Cl^- currents, we used 150µm/l niflumic acid in the bath solution. The pClamp 9 (Axon Instruments) software package was used for data acquisition and analysis. Data were analysed using Molecular Devices Clampfit 10.4 (Sunnyvale, CA) and Microsoft Excel programs. The results were presented as mean$\pm$S.E. For statistical analysis we used GraphPad Prism (San Diego, USA). To choose between parametric or non-parametric tests for normality criteria, we used Shapiro-Wilk estimator. For data sets with small N, we used non-parametric tests to avoid possible type II errors. Mean differences were statistically evaluated using ANOVA with Levene's homogeneity of variances test and pairwise comparisons were made using Turkey adjustment. Non-parametric *k* independent Kruskal-Wallis test was applied with Bonferroni correction to compare the differences among means. Error bars represent $\pm$S.E.

Immunofluorescence

One mL of 70% confluent LCLs in suspension were collected in 1.5mL Eppendorf tube followed a brief centrifugation at 2000rpm for 3 min to collect cells down. Cells were washed briefly once with 1X Phosphate buffer Saline (PBS) and fixed in 4% paraformaldehyde (PFA: P6148, Sigma) for 10 min at RT. Remove PFA traces by washing cells twice with 1X PBS. Primary antibody

incubation was done overnight at 4^{o}C in block solution (0.2% BSA in PBS with 0.02% Triton-X100), while the secondary antibody incubation was done for 2 hrs at RT. Intermediate washing steps were done with PBT (PBS+0.02% Triton-X100) for 30 min. The following antibodies were used; hKir 4.1 (1:1000; Cat no: NBP1-20149, Novus Biologicals), Alexa Fluor 488 phalloidin (1: 1000; A12379: Invitrogen), DAPI (1:5000; D9542: Sigma) and goat anti-mouse IgG Alexa Fluor 488 (1:1000; A11001; Invitrogen). Cells were mounted using Vectashield antifade mounting medium (H-1000: Vector labs) to prevent photobleaching and left overnight at 4^{o}C. Optical *z*-sectioning at 0.2 µM intervals was done using Plan-Apochromat 63x/1.40 oil objective in Zeiss Axio Observer 7 with Apotome 2 feature and Axiocam 702 monochrome camera (Carl Zeiss, Germany). Signal-to-noise ratio was improved using in-built Zeiss deconvolution module and MIP projections of 2-3 *Z*-stacks are presented here. Representative images reported here are from three independent experiments. For quantitative measurements, deconvoluted Z-stacks were first blinded before analysis. 3D surface rendering plugin in Imaris software is used to reduce signal-noise ratio to measure Kir4.1 punctae distribution between cytoplasm and nucleus. The respective numbers were normalized against cytoplasmic space marked by F-actin and nuclear space by DAPI signals.

Experiments with *Drosophila*

***Drosophila* genetics and molecular biology**

Flies were maintained on standard medium at 25^{o}C. w^{1118} strain was used as wild-type control. A EP insertion in *irk2* locus (G8696) obtained from Bloomington Stock Center is imprecisely excised to generate *irk2* mutant alleles by standard procedures. Following fly stocks were used in this study: C155-Gal4 (Lin and Goodman, 1994), TH-Gal4 (Friggi-Grelin et al., 2003), UAS mcd8-eGFP (Jan lab). To assess the effect of *irk2* mutant on the expression levels of irk2, we extracted RNA from embryos (for homozygous $irk2^{e118}$) and larvae (homozygous $irk2^{e91b}$ *and* heterozygous $irk2^{e118/e91b}$) and reverse-transcribed into cDNA. Following primers were used to investigate Irk2 expression levels; CGACGAGAACTCACCGCTCT and AGGGATTCCGCACACCAGCT. Full-length cDNA for Irk2 was amplified using cDNA specific primers [ATGCAGGTCCCGCTCAGCGA and GCAGCTCTCGGTGCCCTTGTAA] and Kir4.1 cDNA obtained from OriGene (SC118741). Site-directed mutagenesis was performed with Irk2 and Kir4.1 cDNA using GeneArtTM site-directed mutagenesis system (A13282: Invitrogen) to generate $Irk2^{T290A}$ and $Kir4.1^{T290A}$ cDNAs. All four cDNAs, described above, were subcloned into fly pUAST transformation vector (Brand and Perrimon, 1993) using Not1 site and used to generate transgenic flies in w^{1118} genetic background.

Larval locomotor assay

Five wandering third-instar larvae, staged appropriately, are placed on 1% agar plate. The total area available for larvae to crawl around is 6 cm (inner diameter of plate). Before recording their locomotor patterns, they were acclimatized for 2 min in the testing arena and recorded for 5 min using 13-megapixel Sony digital camera. The distance from agar plate to camera is 25cm and the entire chamber is enclosed to prevent external light. A LED light source was used underneath agar slabs. The video file was converted into image stacks of 3 fps for 3 min resulting in 5400 frames. Eight such videos were taken from three replicate bottles resulting in 24 videos per group and 120 individual larvae per group. These stacks of images were then analysed using wrMTrck software standardized for *Drosophila* larval locomotion (Brooks et al., 2016).

Live imaging of adult locomotion using flyBowl assay and vertical climbing assay

The schematic of testing arena and the methods to assay adult locomotion are reported in Simon and Dickinson, 2010 (flyBowl assay) and Aggarwal et al., 2018 (vertical climbing assay). We used 3-5 days old flies, aged at 23^{o}C at 12-12 LD cycle. The videos were captured at 250FPS at 0.055mm/pixel resolution using Pointgrey camera (13Y3M) with a Canon 18-55ES lens at 55um/pixel resolution. Total distance traveled: Distance traveled by a fly is equal to the sum of all track lengths in body length units (BLUs) in a given time duration. For a genotype, total distance traveled in a given time is calculated as the mean of total distance traveled by each fly of that genotype. Average speed: For each track, the speed of the fly is calculated as the average instantaneous speed for that track. Further, mean speed of a fly is given by the mean of speeds for all tracks. Finally, for a genotype, average speed is calculated as the mean of mean speed of each fly. For fly bowl Assay: The average speed of the fly was measured by dividing total distance traveled by a fly in a given amount of time. The videos were captured at 15FPS at 0.064mm/pixel resolution. Live imaging done using FlyCon Tra (Fly Contour based Tracker) software (Aggarwal et al., 2018). Statistical analysis of all raw data gathered over time for both fly bowl and vertical climbing assay was done using GraphPad Prism (San Diego, USA). Graphs were plotted using matplotlib library in *Python*. Unpaired t-test (for normal distribution) or Mann-Whitney test (for non-normal distribution) was used for comparison between two genotypes. For comparison between more than two genotypes, we used two-way repeated measures ANOVA, post-hoc Sidak's multiple comparisons. Data is reported as mean$\pm$SEM for all experiments.

Results

Clinical and biochemical features of family with SeSAME syndrome

Six affected individuals were identified from the relatives of an index subject (IV.2) who had sought help with the symptoms of seizures, ataxia and developmental delay. The clinical features were broadly similar to SeSAME syndrome but without electrolyte imbalance (Fig. 1A; Table 1). Born through two consanguineous unions with no perinatal or postnatal problems, all affected individuals developed tonic-clonic seizures at 4-5 months of age and had delayed speech and motor development. Cerebellar symptoms (gait ataxia, intentional tremors and dysdiadochokinesia) were manifested from early childhood. The gait ataxia was progressive in nature, resulting in severe disability and later being confined to wheel chairs [IV. 2-5]. Dysmorphic facies, dysarthria, brisk deep tendon reflexes (DTRs), bilateral ankle clonus and an extensor Babinski response were evident in all of them. All the patients showed certain characteristic dysmorphic facial features like prominent supraorbital ridges, thick eyebrows, deep set eyes, epicanthal fold, low set ears, prominent antihelix, prominent nasal tip and thick lips (Fig. 1B). Behavioural abnormalities like stereotypies, hyperactivity, anger outbursts and psychotic symptoms were also observed (Table 1). They also had hearing impairment, and audiometry measures revealed bilateral mild to severe sensory neural hearing loss. Motor nerve conduction velocities from patients (V.1-2) were normal. The EEG from patients (V.1-2) showed generalised seizure discharges before treatment (Figure 1C), which became normal after treatment with anti-epileptic drugs. The other four members (IV.2-5) remained seizure free for several years on medication. MRI from IV.2 showed enlarged basal ganglia and cerebellar atrophy (Fig. 1D). The remaining members of the family were clinically unaffected.

Various biochemical parameters were evaluated for the six affected individuals (Supplementary Table 1). The raw values of each parameter were unit variance normalized (-1.85 to +1.95) across six samples and hierarchically clustered (Fig. 1F). Serum creatinine levels were highest in III.11 and lowest in III.12. Urinary sodium, serum potassium, serum calcium, serum homocysteine and LDL/HDL ratio were higher in IV.2 compared to remaining individuals. The serum chloride, urinary chloride, plasma ammonia, plasma lactate, vitamin B12, total cholesterol, urinary potassium, blood urea and urinary calcium were relatively higher in III.12 compared to remaining individuals. Aryl sulfatase and urinary creatinine levels were higher in IV.2 and IV.3. Calcium/creatinine and alkaline phosphatase levels were higher in IV.4 and IV.5 compared to remaining individuals.

Novel *KCNJ10*^{T290A} variant residing in a ROH of Chr1 segregate in all patients

To identify the crucial disease-causing loci, we performed WES and analyzed exome-wide levels of homozygosity in all family members. A novel variant *KCNJ10*^{T290A} seems to be cosegregating with a long homozygous stretch in Chr1 in all affected individuals of this kindred (Fig. 2A). Deleterious genetic effects of inbreeding are evident in children's born out of consanguineous unions with a relatively higher burden of homozygous alleles (Bittles and Black, 2010; Shawky et al., 2013; Corry, 2014; Fareed and Afzali, 2014). These effects have been implicated to influence the evolution of mental illness and neurodevelopmental disorders (Bittles and Black, 2010). Since SeSAME syndrome follows autosomal recessive (AR) inheritance and the role of homozygous alleles in AR illness has been well established (Sund et al., 2013; Kelmemi et al., 2015; Wang et al., 2016; Martin et al., 2018), we used two independent approaches to identify the causative variants segregating with the illness in the SeSAME family; assessing the exome-wide runs of homozygosity (ROH), referred as ROH method and assessing the variants based on their allele frequencies, referred as non-ROH method.

Variant prioritization using ROH method

We analyzed the exome-wide levels of homozygosity for all samples within the pedigree including seven population controls (see materials and methods). Principal Component Analysis (PCA) of the exome-wide F-statistics separates the family members (n=6) from the population controls (n=7), explaining for an overall variance of 49.6%. All samples (both familial and population) within the two clusters, fell within their 95% confidence ellipses, except for 2 controls representing the relatively admixed communities (Fig. 2B). The SeSAME family alone was subjected to PCA in which the cases (n=4) formed a cluster and the unaffected parents (n=2) fell outside the 95% confidence ellipse (Supplementary Fig. 2), explaining the intra-familial variance in homozygosity. The ROH within the exomes of the individuals in the pedigree and the population controls were identified. A total of 56 homozygous stretches (either overlapping or unique) were identified in all cases and controls, of which 44 stretches belonged to the four affected siblings and the remaining were distributed between unaffected parents and population controls (Supplementary Table 2). Nevertheless, no ROH was detected in a subset of population controls. The burden of ROHs witnessed in the cases as compared to controls could be attributed to their consanguineous parentage. Of the ROHs identified in total, five stretches were explicitly shared between all the affected siblings but not observed in the unaffected parents and population controls, which will henceforth be notified as $ROH_{affected}$ (Table 2). The $ROH_{affected}$ consists of a union set of 5329 variants across all the cases and controls, of which any given variant was observed in at least one sample. Since the disorder follows an autosomal recessive (AR)

inheritance pattern, of the 5329 variants, we identified those that were heterozygous (HET) in both unaffected parents, but homozygous (HOM) in all of the affected siblings. Seventy-eight such variants, belonging to 47 genes, were identified and all of them mapped to Chr 1 (Supplementary Table 3). This skewed observation could not be attributed to the length of Chr 1 for three reasons: i) the method used to compute ROH uses a sliding window approach which essentially removes the bias induced by the length of the chromosome; ii) the same Chr 1 ROH was not observed in either of the controls; iii) no ROH was observed in Chr 2 despite its genomic length being comparable to that of Chr 1. Of the 78 variants only three missense variants i.e., i) Chr1:158368964-C-T (*OR10T2*) ii) Chr1:160011455-T-C (*KCNJ10*) and iii) Chr1:161495040-C-T (*HSPA6*), were predicted to be deleterious by both SIFT (Vaser et al., 2016) and PolyPhen (Adzhubei et al., 2015).

Variants prioritization using non-ROH method

To identify other putative deleterious variants segregating within the family, which could have otherwise been ignored by the ROH based method, we identified all the exonic and splice variants (including non-synonymous, stop gain and stop loss) segregating within the family. The common variants i.e., those with a minor allele frequency (MAF)>0.01 in 1KG_all (1000 Genomes Project) and ExAC_all (Exome Aggregation Consortium) databases, were excluded from the analysis (Clarke et al., 2012; Lek et al., 2016). We identified seven variants belonging to seven genes (Supplementary Table 4). Interestingly, all the seven variants were located within Chr1:151288779-161088292, which was a subset of $ROH_{affected.}$ Amongst the seven variants, Chr1:160011455-T-C [*KCNJ10*] was an obvious overlap. The remaining six variants fell on *PI4KB, RORC, FLG2, FCRL1, PVRL4* and *NIT1* genes. Apart from the *KCNJ10* variant, none were predicted to be deleterious by both SIFT and PolyPhen. However, three of the remaining six variants (Chr1:151288779-T-C [*PI4KB*], Chr1:161049499-G-A [*PVRL4*] and Chr1:161088292-A-G [*NIT1*]) were predicted to be deleterious by either of the two algorithms, and were seemingly rare with MAFs of 0, 3E-3 and 5E-3 respectively, in South Asian populations according to the gnomAD database (Lek et al., 2016). Finally, the zygosity of the $KCNJ10^{T290A}$ variant was confirmed for all individuals in the family (III.11-12, IV.2-5, IV.9-10 and V.1-2) by Sanger sequencing (Fig. 2C).

Thus, of the union set of nine putative deleterious variants (three based on ROH method and seven based on allele frequencies) segregating within the family, the *KCNJ10* gene was shortlisted for functional analysis to unravel the molecular impact of the variant for following reasons: i) *KCNJ10*, the candidate gene known to cause SeSAME syndrome (Celmina et al., 2018); ii) the variant reported in the patients is novel; iii) this was the only deleterious variant identified by both methods and iv) the variant resides on the cytoplasmic C-terminal tail (Fig. 2D) which is strongly conserved through evolution (Fig. 2E).

Kir4.1^{T290A} disrupts channel properties in patient-derived LCLs

LCLs have been routinely used as a surrogate *in vitro* cell model to investigate cellular mechanisms of neurodevelopmental psychiatric disorders (Giuliano et al., 2014; Kumar et al., 2016). To investigate the functional role of Kir4.1^{T290A}, we generated patient-specific LCLs, validated by karyotype for six members of SeSAME family. All six LCLs are free from both numeric and structural chromosomal abnormalities (Supplementary Fig. 1).

The barium-sensitive inwardly-rectifying K^+ current in LCLs measured by whole-cell patch clamp was substantially compromised in all affected individuals. Kir4.1^{T290A} significantly depolarized membranes of LCL and showed deficits in clearance of extracellular K^+. To determine whether LCLs express functionally active endogenous Kir4.1 protein, we used immunofluorescence (IF), western blot and electrophysiology (Fig. 3). In parental controls, Kir4.1 is in close proximity with the actin-rich plasma membrane, diffusely discernible in the cytoplasm and enriched in the nuclear membrane and nucleus (Fig. 3A). However, in all affected individuals, we observed an increased punctate distribution of Kir4.1 in the cytoplasm but with no apparent disparity in the nucleus and nuclear membrane (Fig. 3B). To confirm the IF findings, western blot analysis showed a substantial increase in the expression of Kir4.1 in all affected individuals compared with unaffected parents (Fig. 3C and 3D). These findings suggest an unstable nature of Kir4.1^{T290A} in all affected individuals.

To confirm whether the endogenous Kir4.1 expressed in LCLs is functionally active and elicit detectable inward-rectifying potassium currents *in vitro*, we performed whole-cell patch clamp recordings in response to voltage-steps from -120 to 40mV in 10mV, from a holding potential of -30mV both in the presence and absence of 110µM barium, a selective Kir channel blocker. Baseline current discharges from two heterozygous parental controls (III.11: -0.89$\pm$0.086, n=18, p=1.114 and III.12: -0.86$\pm$0.049, n=16, p=1.347) were not significantly different from wild type controls (-0.85$\pm$0.046, n=17) (Fig. 3E). In contrast, the average barium-sensitive current densities were substantially decreased in all three control LCLs tested, in heterozygous parents (III.11: -0.64$\pm$0.041, n=15, p=2.1E-4 and III.12: -0.60$\pm$0.086, n=14, p=1.8E-4) and wild type (-0.63$\pm$0.104, n=14, p=2.5E-4) compared with their respective baseline discharges, implying the specificity of K^+ currents recorded from endogenous Kir channels (Fig. 3E).

We recorded the resting membrane potential of LCLs from patients (Fig. 3F). Average membranes voltages from all patients (IV.2: -30mV$\pm$3.640, n=18, p=1.3E-5; IV.3: -32mV$\pm$2.156, n=20, p=2.4E-5; IV.4: -31mV$\pm$3.083, n=17, p=1.7E-4; IV.5: -24mV$\pm$2.817, n=20, p=2.8E-5) were significantly hyperpolarized as compared to wild type (WT:-55mV$\pm$4.102, n=24) and parental controls (III.11: -51mV$\pm$3.842, n=21 and III.12: -50mV$\pm$4.21, n=19). In whole-cell voltage clamp, membrane current amplitudes were measured in all family members at both positive and negative potentials than the K^+ equilibrium potential (E_k) (Fig. 3G and 3H). The mean current densities as a function of voltage (pA/pF) measured in all those expressing the mutant channel were markedly smaller than wild type and parental controls (Fig. 3H). One major facet of the Kir4.1 channel is to clear extracellular K^+ thereby showing stronger rectification. To test the K^+ clearance ability of LCLs, we clamped the cells at their resting membrane potential, with and without 110µM barium, and measured the elicited membrane current discharges upon induced K^+ steps (from 5-20 mM). Overall, barium-sensitive currents from all patients were significantly reduced when compared to both parental and wild type controls (Fig. 3I).

Neural expression of Kir4.1^{T290A} did not rescue *Drosophila irk2* mutant phenotypes

Of the three Kir channel proteins expressed in *Drosophila*, BLASTp search identified Irk2 (CG4370), as the single closest homolog of human Kir4.1. Amino acid sequence alignment of Irk2 with Kir4.1 showed identical domain organization with 20% identity and 36% similarity (Fig. 4A). Enhancer-promoter (EP) element G8696 residing in the intronic region of Irk2 genomic locus was imprecisely excised to generate a 2348 bp and 2092 bp deletion from the EP

insertion site to the pore-forming intramembrane domain, yielding two *irk2* mutant alleles; $irk2^{e118}$ and $irk2^{e91b}$ (Fig. 4B). Homozygous $irk2^{e118}$ mutants are late embryonic lethal and transcriptional null allele, whereas homozygous $irk2^{e91b}$ mutants hatched viable and fertile adults with 51±12% reduction in Irk2 mRNA levels relative to wildtype and hemizygous genetic controls (Fig. 4C). However, the transheterozygotes ($irk2^{e118}$/ $irk2^{e91b}$); henceforth referred as *irk2* mutant, exhibited reduction in Irk2 mRNA levels (72±15%) and shortened life span (Fig. 4D). Furthermore, to confirm the specificity of *irk2* whole mutant phenotypes, we performed rescue experiments using the Gal4-UAS system with $Irk2^{WT}$, $Kir4.1^{WT}$, $irk2^{T290A}$ and $Kir4.1^{T290A}$ channel proteins. Motor neuron-specific overexpression of either $Irk2^{WT}$ or $Kir4.1^{WT}$, substantially rescued embryonic lethality of $irk2^{e118}$ homozygous mutants and shortened life span of heteroallelic *irk2* mutant. The neural specific overexpression of mutant proteins $irk2^{T290A}$ and $Kir4.1^{T290A}$, in contrast, failed to ameliorate *irk2* mutant phenotypes (Fig. 4E).

In addition, we assayed larval locomotion to study the inherent functional capacity of Irk2 channels in motor neurons. Live imaging of larval locomotion over time followed by automated tracing revealed substantial restricted movement of *irk2* compared to WT controls (Fig. 5A). *irk2* (n=100) mutants displayed altered peristaltic behaviour (26±6.8) and speed (5.9±0.2) compared to WT (n=100; 75±5.9, $p<0.00024$ and 2.4±0.32, $p<0.00017$, respectively). Both peristaltic and speed defects are substantially improved by restoring $Irk2^{WT}$ channel expression (57±7, n=100, $p<0.00035$ and 5.4±0.16, n=100, $p<0.00054$) and $Kir4.1^{WT}$ (59±5.3, n=100, $p<0.00017$ and 5.8±0.23, n=100, $p<0.00068$) in neurons (Fig. 5B). Nonetheless, neural expression of mutant proteins *viz*., $irk2^{T290A}$ and $Kir4.1^{T290A}$ failed to suppress the locomotor defects of *irk2* implying the functional significance of T290A mutation segregating in SeSAME family (Fig. 5).

irk2 mutant flies displayed impaired locomotion

The motor neurons in adult flies are necessary for complex movements (Bidaye et al., 2014; Enriquez et al., 2015; Gowda et al., 2018) and we tested the persistence of early larval phenotypes in young adults. We used high-resolution live-tracking adult locomotor assays in two independent platforms; a vertical fly-climbing assay to measure fly's innate response to gravity and its role in patterns of locomotion, thereby indirectly assaying the drive to move (Fig. 6A; Aggarwal et al., 2018) whereas horizontal fly-bowl assay which measures locomotion in a cue free environment (Fig. 6D; Simon and Dickinson, 2010). In the vertical fly-climbing assay, 5-day old flies were provided with regular stimulus for locomotion by rotating the arena for fly climbing every 15 seconds (Aggarwal et al., 2018). The innate geotactic response of the flies makes them always climb towards the top of the arena, and when, after 15 seconds, the arena is rotated 180 degrees, the flies which are on the top are now pushed downwards providing them with the geotactic stimulus. This regular geotactic stimulus, delivered every 15 seconds is processed very reliably in the controls, with an evident climbing event for each rotation. *irk2* mutants, are positively geotactic in the first minute (p=0.02; data not shown). The total number of tracks as well as the distance remain unchanged between wild type and *irk2* mutants (p=0.3788; p=0.4656). However, the average time spent by flies per track was higher in *irk2* mutants (7.98±0.44 seconds) compared with wild type (5.83±0.65 seconds, p=0.0183, unpaired student's t-test, n=10; Fig. 6B). Furthermore, *irk2* mutants were slow climbers (1.56 ± 0.15 BLU/s) compared to controls (2.36 ±0.22 BLU/s, p=0.0095, unpaired student's t-test, n=10) (Fig. 6C; Supplementary Video 1). In the flyBowl assay, *irk2* mutants walked significantly slower (2.49±0.28 mm/s) as compared to wild type (4.24±0.35mm/s, p=0.002, unpaired Kolmogorov-

Smirnov test, Fig. 6E). In this cue free environment, the *irk2* mutants showed a sharp decline in locomotor activity post 6 minutes into the assay compared to wild type flies ($p<0.01$ for all the time points, two-way repeated measures ANOVA, post-hoc Sidak's multiple comparisons, $n>35$, Supplementary Video 2).

Progressive loss of dopaminergic neurons in the *irk2* mutant brain

We know that specific loss of dopaminergic neurons in the aging brain lead to motor deficits in many neurodegenerative conditions especially in Parkinsonism and Ataxia syndrome. In addition, these patients manifested tremors, ataxia, progressive spasticity and basal ganglia and cerebella dysfunction. We therefore explored whether a similar pathology occurs in *irk2* mutants. To visualize DA neurons in 30 days old adults, we used TH (tyrosine hydroxylase)-specific Gal4 line (Friggi-Grelin et al., 2003) fused to membrane-tethered eGFP. Cells positive for anti-GFP were consider for analysis. We focused on six major clusters in central brain, which are annotated hereafter as paired posterior lateral 1 and 2 (PPL1 and PPL2); paired posterior media 1 and 2 (PPM1/2), paired posterior medial 3 (PPM3) and paired anterior lateral (PAL) (Fig. 7A). Paired anterior media (PAM) cluster was excluded from our analysis, since TH-Gal4 does not reliably label these cells. The neurons in all four DA clusters per hemisphere were significantly fewer in *irk2* mutant flies, as compared to age-matched controls (Fig. 7B). This suggests that inhibiting Irk2 channel function promotes degeneration of DA clusters. To test whether the observed decrease in DA neurons is due to age-associated neurodegeneration rather an improper neural development, we analysed DA clusters in these mutants at an early age. On day 3, *irk2* mutants showed no loss DA neurons compared to age-matched control flies (Fig. 7C). These results, strongly suggest that loss of *irk2* function is sufficient to accelerate age-dependent progressive loss of dopaminergic neuronal clusters which could plausibly be attributed to locomotor defects and shortened-life span.

Discussion

We are able to identify a novel variant in the *KCNJ10* gene as a cause for the SeSAME syndrome. The biological processes involved were explored using genomics, channel physiology from patient-derived LCLs and behavioural abnormalities in *Drosophila* that are influenced by age-dependent degeneration of dopaminergic neurons. These processes are perhaps conserved across species, and could provide a useful platform for translational neuroscience (Ryczko and Dubuc, 2017; Splinter et al, 2018).

Why renal tubulopathy is spared in a subset of SeSAME cases?

All six affected individuals in SeSAME family reported here displayed relatively uniform neurological and psychiatric manifestations in the form of ataxia, focal epilepsy, delayed developmental milestones, loss of intellectual and sensory-neural hearing but with no apparent electrolyte imbalance. These clinical features specific to SeSAME-like pedigrees (Dhaibani et al., 2018) is also evident in children with autism-spectrum disorders with epilepsy (Sicca et al., 2011; Sicca et al., 2016). In fact, several modern-day mammals like Jack Russell Terriers (Gilliam et al., 2014), Belgian Shepherd dogs (Mauri et al., 2017) and Malinois dogs (Van Poucke et al., 2017) experienced this SeSAME-like phenotype with *KCNJ10* mutations. Therefore, it remains obscure how and why certain *KCNJ10* variants fail to manifest electrolyte imbalances in SeSAME syndrome. There could be two possibilities for this discrepancy. First, it's possible that certain *KCNJ10* mutations can affect CNS functions independently of other

organ systems. It is conceivable that astrocytes and microglial cells of nervous system are highly sensitive to dysregulation of potassium homeostasis, while basolateral membrane in the distal nephron may be impervious to this effect (Djukic et al., 2007). Another possibility is that same *KCNJ10* variants could behave differently between CNS and kidney, since the channel activity depends largely on the formation of heterotetramers with other Kir entities (Kir5.1), cell type specificity, gating mechanisms and influence of cell surface signaling receptors (Reichold et al., 2010; deHart et al., 2008). Finally, it is unclear whether renal electrolyte deficit is a progressive impairment that develops over time, or a direct effect of the mutation, which necessitates further investigations and follow-up clinical evaluations.

Is ROH a cause or an effect of recessive inheritance in SeSAME syndrome?

The *KCNJ10* is the single most identified candidate gene for the SeSAME syndrome, with 21 mutations from 27 patients reported till date, of which 11 were from consanguineous unions (Celmina et al., 2018). Autosomal recessive neuropsychiatric illnesses have also been witnessed in children born out of consanguineous marriages and some of them carry long stretches of homozygous segments within their genomes (Melhem et al., 2016; Gandin et al., 2015; Bittles and Black, 2010). Since the affected individuals detected to have SeSAME syndrome were born out of consanguineous parentage, we primarily used the ROH based approach to identify those variants present within the homozygous stretches shared between all those affected. This approach identified three deleterious variants belonging to *KCNJ10, OR10T2 and HSPA6* genes. The allele frequencies of *OR10T2* (18%) and the *HSPA6* (9%) variants in the ExAC South Asian (SAS) populations are fairly high and hence unlikely to contribute to illness. However, it is interesting to note the previous association of the reported *HSPA6* variant in patients with sensory disturbances (Kobayashi et al., 2013). This suggests that although gene of major effect are probably the primary drivers of the illness, the diversity in the clinical presentation is possibly an outcome of the complex genetic interactions between common and rare variants of varying effect sizes. As an alternative, we also used a non-ROH approach which is purely based on the allele frequencies to identify homozygous rare coding variants that could have been missed out by the previous approach. The fact that both methods autonomously converged to a deleterious novel $KCNJ10^{T290A}$ variant, co-segregating with the illness is remarkable. Given the clinical phenotypic diversity and for additional reasons as discussed above, we suggest two possibilities broadly classified into intrinsic and extrinsic factors. Intrinsic factors include recombination hot-spots, defects in DNA repair, chromatin remodelling and yet unidentified intra-cellular signaling events, that favour to the occurrence of ROH, co-segregating with the illness. Another factor could be the clan structure of the family, which indicates a high degree of endogamy. Therefore, an interplay between these two factors could influence the clinical diversity of SeSAME syndrome.

Another possibility is that individual ROHs might play key role in spatial-temporal regulation of gene expression within cell types that are sensitive to K^+ homeostasis (Christofidou et al., 2015). The difference in the expression of Kir4.1 among unaffected siblings in our SeSAME pedigree also highlights the role of ROH in gene regulation. Therefore, it would be useful to investigate the functional consequences of homozygosity in expression of genes within the ROH and/or in close proximity especially in cell types that are relevant to the pathophysiology of SeSAME syndrome.

Usually for every pregnancy in autosomal recessive disorders, there is a probability of 0.25 that the offspring(s) will inherit two copies of the disease gene and will therefore exhibit the phenotype (Ellard et al., 2015). However, in a clinical setting this distribution is skewed more towards almost all affected individuals in the same generation, than one would rather expect by chance, especially in children born to consanguineous unions. Thus, this skewed observation needs to be addressed at holistic paradigms by developing bio-physical and mathematical models to understand the physics and governing dynamics (Nash J.F, 1950) of the intra-cellular events, influencing the silent recombination choices of homologous chromosomes.

Importance of *KCNJ10* variant characterization in SeSAME syndrome

Functional characterization of exogenously expressed mutant Kir4.1 has been attained in a variety of isolated cell types like astrocytoma cells (Sicca et al., 2016), C6 glioma cells (Mendez-Gonzalez et al., 2016), CHO and HEK 293 cells (Reichold et al., 2010; Williams et al., 2010), *Drosophila* S2 cells (Doring et al., 2002), kidney-derived ts201 cells (Mendez-Gonzalez et al., 2016) and Cosm6 (Kucheryavykh et al., 2007). However, the sensitivity and specificity of physiological read outs from Kir ion channels depends inherently on factors like cellular milieu, auxiliary subunits and formation of subunits for heterooligomeric assembly in the cell type of choice (Doring et al., 2002; Neush et al., 2006; Fakler et al., 1996a and 1996b). Another major challenge is to extrapolate the findings from cloned Kir channels in isolated cell types to their native effects in disease-relevant tissues, which most likely yield weak currents and rectification (Olsen et al., 2006). Therefore, *in vitro* cellular models that preserves the native environment to measure authentic Kir4.1 channel activity will serve as an excellent cell of choice to investigate functional effects. We therefore addressed these issues, using patient-derived LCLs which harbour the risk variant.

Since the $KCNJ10^{T290A}$ variant observed in this SeSAME family, is a potential threonine phosphorylation residue, we performed *in silico* analysis to explore this possibility. Using Group-based Prediction system (GPS; Xue et al., 2008), we speculate that T290 could potentially be phosphorylated (GPS score 9.4 > cutoff 6.78 by Interleukin 1 Receptor Associated Kinase 4, IRAK4) at native conditions. Nonetheless, T290A phosphorylation has not been reported in *PhosphoSitePlus*. In light of the *in-silico* predictions and *in vitro* functional implications of $KCNJ10^{T290A}$ variant using patient-derived LCLs followed by whole-cell patch clamp (see results section), we predict the likelihood of T290 phosphorylation either at a very low stoichiometry or under specific signaling stimuli. However future experiments will assist in discriminating between these possibilities.

Genetic manipulation techniques and phenotypic similarities among different categories of K^+ channel mutants in *Drosophila* (Littleton and Ganetsky, 2000; Bellen et al., 2010), offer an excellent opportunity to investigate the functional role of Kir ion channels at organismal level. Apart from *in vitro* approaches, animal models showed greater potential in deciphering the cell-type specific role of Kir4.1 in brain function. Justifying the importance of Kir4.1 in K^+ homeostasis, Kir4.1 knockout mouse, *Xenopus* oocytes and *zebrafish* mimics a subset of SeSAME symptoms observed in humans (Djukic et al., 2007; Neusch et al., 2001). In fact, of the three Kir channels identified in *Drosophila*, reduced expression of irk2 in the CNS lead to defects in spike discharges and adult lethality suggesting an alternate model to investigate cellular functions of Kir4.1 (Chen and Swale, 2018). In addition, irk2 channels are constitutively

active in *Drosophila* S2 cells, derived from the macrophage-like lineage, and functionally associate with sulphonyl urea receptors (SUR). In this study, we explored the role of Irk2 in CNS at cellular level. Irk2 is essential for survival of adult dopaminergic neurons and for coordinated rhythmic locomotion in larval and adult motor neurons. This relies on complex interplay between central and peripheral nervous systems where the central pattern generator (CPG) neurons at neuromeres regulate peristaltic movement of peripheral body wall muscles (Hasegawa et al., 2016; Kohsaka et al., 2017). Therefore, it appears that Irk2 ion conductance pathway in *Drosophila* is responsible for regulating K^+ gradient and glutamate homeostasis at tripartite synapses of neuromuscular junctions (NMJ) ultimately controlling synaptic activity and neurotransmitter release. In addition, it would be valuable to dissect the role of Irk2 in synaptic vesicle turnover at NMJ given the role of K^+ inward rectification in regulating endocytosis (Feliciangeli et al., 2010). Finally, our findings provide a proof-of-concept approach to explore the cell type specific function of Kir4.1 in *Drosophila* nervous system to better understand mechanisms of K^+ spatial buffering and synaptic architecture which is an essential feature for proper synaptic transmission and plasticity.

Finally, recapitulating the biology of complex neuropsychiatric disorders in cellular and animal models, to identify downstream mechanisms is of heuristic value. Using patient-specific cells we were able to show the dysfunction of the primary disease causative gene in SeSAME syndrome, which when defective can cause quantifiable degenerative symptoms in *Drosophila* model system. As we constantly expand the identification of candidate genes for neuropsychiatric syndromes, these trans-disciplinary approaches will benefit our understanding of genotype-phenotype correlations at mechanistic level.

Acknowledgement

The authors are immensely grateful to all members of SeSAME family for their participation and constant involvement in this study. This work was primarily carried out by NIMHANS in collaboration with Prof. K. VijayRaghavan's lab at National Centre for Biological Sciences, Tata Institute of Fundamental Research (NCBS – TIFR). We thank Jan's lab (UCLA), Prof. LS Shashidhara's lab (IISER, Pune), Edward Giniger's lab (NINDS), Bloomington Stock centre for generous sharing of fly stocks and reagents and Gautham (NIMHANS) for facial description of SeSAME kindreds. We are grateful to Prof. K.VijayaRaghavan for helpful discussion during the course of investigation. We thank ADBS genomic team for sharing the WES analysis pipeline. This work was generously supported with funds from Ramalingaswami re-entry fellowship (RLF/DBT/2015), ADBS (BT/PR17316/MED/31/326/2015) from Department of Biotechnology and Department of Science and Technology (ECR/2015/000468) and National Centre for Biological Sciences, Tata Institute of Fundamental Research. Finally, the authors are thankful to all members of the lab and the ADBS consortium for suggestions and discussions during the course of investigation.

Funding

These experiments were supported by Ramalingaswami re-entry fellowship (RLF/DBT/2015) and ADBS (BT/PR17316/MED/31/326/2015) from Department of Biotechnology; Early career grant (ECR/2015/000468) from Department of Science and Technology and National Centre for Biological Sciences, Tata Institute of Fundamental Research.

Authors contributions

Conceptualization: RK
Special methodology: RKN, AC, RPM, VVP, SJ and JS
Investigation: RKN, AC, AA, AGS, SS, SP, MD, NR, MP, PSB, BV, MN, BM and RK
Manuscript writing: RKN, AC and RK
Data visualization and analysis: RKN, AC, AA and RK
Supervision: RK

Competing interests

The authors declare no competing or financial interests.

References

Adzhubei I, Jordan DM, Sunyaev SR. Predicting functional effect of human missense mutations using PolyPhen-2. Curr Protoc Hum Genet 2013; 214-225.

Aggarwal A, Reichert H and VijayRaghavan K. A cost-effective high-resolution climbing assay applied to *Drosophila* Parkinson's and proprioception mutants reveal novel behavioral phenotypes. 2018; https://doi.org/10.1101/426544.

Ahmed P, Vidhya V, et al. INDEX-db: The Indian Exome Reference database (Phase-I). biorxiv. 2018. doi: https://doi.org/10.1101/312090

Bellen HJ, Tong C, Tsuda H. 100 years of Drosophila research and its impact on vertebrate neuroscience: a history lesson for the future. *Nat Rev Neurosci*. 2010;11(7):514-22.

Bidaye SS, Machacek C, Wu Y, Dickson BJ. Neuronal control of Drosophila walking direction. Science. 2014; 344(6179):97-101.

Bittles AH, Black ML. Evolution in health and medicine Sackler colloquium: Consanguinity, human evolution, and complex diseases. Proc Natl Acad Sci U S A. 2010; 26:107.

Bockenhauer, D., Feather, S., Stanescu, H. C., Bandulik, S., Zdebik, A. A., Reichold, M., et al. Epilepsy, ataxia, sensorineural deafness, tubulopathy, and KCNJ10 mutations. N. Engl. J. Med. 2009; 360: 1960–1970.

Brand AH, Perrimon N. Targeted gene expression as a means of altering cell fates and generating dominant phenotypes. Development. 1993; 118(2):401-15.

Brickshawana, A., Hinson, S. R., Romero, M. F., Lucchinetti, C. F., Guo, Y., Buttmann, M., et al. Investigation of the KIR4.1 potassium channel as a putative antigen in patients with multiple sclerosis: a comparative study. Lancet Neurol. 2014; 13: 795–806.

Brooks DS, Vishal K, Kawakami J, Bouyain S, Geisbrecht ER. Optimization of wrMTrck to monitor *Drosophila* larval locomotor activity. J Insect Physiol. 2016; 93-94:11-17.

Buono RJ, Lohoff FW, Sander T, Sperling MR, O'Connor MJ, Dlugos DJ, Ryan SG, Golden GT, Zhao H, Scattergood TM, Berrettini WH, Ferraro TN. Association between variation in the human KCNJ10 potassium ion channel gene and seizure susceptibility. Epilepsy Research 2004; 58:175–183.

Celmina M, Micule I, Inashkina I, Audere M, Kuske S, Pereca J, Stavusis J, Pelnena D, Strautmanis J. EAST/SeSAME syndrome: Review of the literature and introduction of four new Latvian patients. Clin Genet. 2018 May 3.

Chen R, Swale DR. Inwardly Rectifying Potassium (Kir) Channels Represent a Critical Ion Conductance Pathway in the Nervous Systems of Insects. Sci Rep. 2018; 8(1):1617.

Christofidou P, Nelson CP, Nikpay M, et al. Runs of Homozygosity: Association with Coronary Artery Disease and Gene Expression in Monocytes and Macrophages. Am J Hum Genet. 2015; 97(2):228-37.

Clarke L, Zheng-Bradley X, Smith R, et al. The 1000 Genomes Project: data management and community access. Nat Methods. 2012; 9(5):459-62.

Corry PC. Consanguinity and prevalence patterns of inherited disease in the UK Pakistani community. Hum Hered. 2014; 77(1-4): 207-16.

Danecek P, Auton A, Abecasis G, et al. The variant call format and VCFtools. Bioinformatics. 2011; 27(15):2156-8.

deHart GW, Jin T, McCloskey DE, Pegg AE, Sheppard D. The alpha9beta1 integrin enhances cell migration by polyamine-mediated modulation of an inward-rectifier potassium channel. Proc Natl Acad Sci U S A. 2008;105(20):7188-93.

Dhaibani MA, El-Hattab AW, Holroyd KB, Orthmann-Murphy J, Larson VA, Siddiqui KA, Szolics M, Schiess N. Novel mutation in the KCNJ10 gene in three siblings with seizures, ataxia and no electrolyte abnormalities. J Neurogenet. 2018; 32(1):1-5.

Djukic B, Casper KB, Philpot BD, Chin LS, McCarthy KD. Conditional knock-out of Kir4.1 lead to glial membrane depolarization, inhibition of potassium and glutamate uptake, and enhanced short-term synaptic potentiation. J Neurosci. 2007; 27:11354–11365.

Döring F, Wischmeyer E, Kühnlein RP, Jäckle H, Karschin A. Inwardly rectifying K+ (Kir) channels in Drosophila. A crucial role of cellular milieu factors Kir channel function. J Biol Chem. 2002: 12;277(28):25554-61.

Ellard S, Kivuva E, Turnpenny P, et al. An exome sequencing strategy to diagnose lethal autosomal recessive disorders. Eur J Hum Genet. 2014; 23(3):401-4.

Enriquez J, Venkatasubramanian L, Baek M, Peterson M, Aghayeva U, Mann RS. Specification of individual adult motor neuron morphologies by combinatorial transcription factor codes. Neuron. 2015; 86(4):955-970.

Fakler B, Bond CT, Adelman JP, Ruppersberg JP. Heterooligomeric assembly of inward-rectifier K+ channels from subunits of different subfamilies-Kir 2.1 (Irk1) and Kir 4.1 (Bir10). Pflugers Archiv - Eur J Physiol; 1996a: 433:77-83.

Fakler B, Schultz JH, Yang J, Schulte U, Brändle U, Zenner HP, Jan LY, Ruppersberg JP. Identification of a titratable lysine residue that determines sensitivity of kidney potassium channels (ROMK) to intracellular pH. EMBO Journal. 1996b; 16:4093–4099.

Fareed M, Afzal M. Estimating the inbreeding depression on cognitive behavior: a population-based study of child cohort. PLoS One. 2014; 9(10): e109585.

Feliciangeli S, Tardy MP, Sandoz G, et al. Potassium channel silencing by constitutive endocytosis and intracellular sequestration. J Biol Chem. 2009;285(7):4798-805.

Friggi-Grelin F, Coulom H, Meller M, Gomez D, Hirsh J, Birman S. Targeted gene expression in Drosophila dopaminergic cells using regulatory sequences from tyrosine hydroxylase. J Neurobiol. 2003; 54(4):618-27.

Gandin I, Faletra F, Faletra F, Carella M, Pecile V, Ferrero GB, Biamino E, Palumbo P, Palumbo O, Bosco P, Romano C, Belcaro C, Vozzi D, d'Adamo AP. Excess of runs of homozygosity is associated with severe cognitive impairment in intellectual disability. Genet Med. 2015; 17(5):396-9.

Gilliam D, O'Brien DP, Coates JR, et al. A homozygous KCNJ10 mutation in Jack Russell Terriers and related breeds with spinocerebellar ataxia with myokymia, seizures, or both. J Vet Intern Med. 2014; 28(3):871-7.

Giuliano S, Agresta AM, De Palma A, et al. Proteomic analysis of lymphoblastoid cells from Nasu-Hakola patients: a step forward in our understanding of this neurodegenerative disorder. PLoS One. 2014; 9(12):e110073.

Gowda SBM, Paranjpe PD, Reddy OV, et al. GABAergic inhibition of leg motoneurons is required for normal walking behavior in freely moving *Drosophila*. Proc Natl Acad Sci U S A. 2018;115(9): E2115-E2124.

Gu C. KIR4.1: K^+ Channel Illusion or Reality in the Autoimmune Pathogenesis of Multiple Sclerosis. Front Mol Neurosci. 2016; 9:90.

Hasegawa E, Truman JW, Nose A. Identification of excitatory premotor interneurons which regulate local muscle contraction during *Drosophila* larval locomotion. Sci Rep. 2016; 6:30806.

Heuser K, Nagelhus EA, Taubøll E, Indahl U, Berg PR, Lien S, Nakken S, Gjerstad L, Ottersen OP. Variants of the genes encoding AQP4 and Kir4.1 are associated with subgroups of patients with temporal lobe epilepsy. Epilepsy Research 2010; 88:55–64.

Hibino H, Inanobe A, Furutani K, Murakami S, Findlay I, Kurachi Y. Inwardly rectifying potassium channels: Their structure, function, and physiological roles. Physiol Rev 2010; 90:291–366.

Higashi K, Fujita A, Inanobe A, Tanemoto M, Doi K, Kubo T, Kurachi Y An inwardly rectifying K^+ channel, Kir4.1, expressed in astrocytes surrounds synapses and blood vessels in brain. Am J Physiol Cell Physiol. 2001 Sep;281(3):C922-31.

Howe B, Umrigar A, Tsien F. Chromosome preparation from cultured cells. Journal of visualized experiments: JoVE. 2014(83).
Hui-Yuen J, McAllister S, Koganti S, Hill E, Bhaduri-McIntosh S. Establishment of Epstein-Barr virus growth-transformed lymphoblastoid cell lines. Journal of visualized experiments: JoVE. 2011(57).

John F. Nash Jr. Equilibrium points in n-person games. PNAS;1950 36 (1) 48-49.

Kahanovitch U, Cuddapah VA, Pacheco NL, Holt LM, Mulkey DK, Percy AK, Olsen ML. MeCP2 Deficiency Leads to Loss of Glial Kir4.1. eNeuro. 2018: 19; 5(1). 0194-17.

Kelley KW, Ben Haim L, Schirmer L, et al. Kir4.1-Dependent Astrocyte-Fast Motor Neuron Interactions Are Required for Peak Strength. Neuron. 2018; 98(2):306-319.e7.

Kelmemi W, Chelly I, Kharrat M, Chaabouni-Bouhamed H. Consanguinity and homozygosity among Tunisian patients with an autosomal recessive disorder. J Biosoc Sci. 2015; 47(6):718-26.

Kobayashi D, Nishizawa D, Takasaki Y, et al. Genome-wide association study of sensory disturbances in the inferior alveolar nerve after bilateral sagittal split ramus osteotomy. Mol Pain. 2013; 9:34.

Koboldt DC, Larson DE, Wilson RK. Using VarScan 2 for Germline Variant Calling and Somatic Mutation Detection. Curr Protoc Bioinformatics. 2013; 44:15.4.1-17.

Kofuji P, Ceelen P, Zahs KR, Surbeck LW, Lester HA, Newman EA. Genetic inactivation of an inwardly rectifying potassium channel (Kir4.1 subunit) in mice: phenotypic impact in retina. J Neurosci. 2000; 20:5733–5740.

Kohsaka H, Guertin PA, Nose A. Neural Circuits Underlying Fly Larval Locomotion. *Curr Pharm Des.* 2017;23(12):1722-1733.

Kucheryavykh YV, Pearson WL, Kurata HT, Eaton MJ, Skatchkov SN, Nichols CG. Polyamine permeation and rectification of Kir4.1 channels. Channels (Austin). 2007;1(3):172-8.

Kumar S, Curran JE, Glahn DC, Blangero J. Utility of Lymphoblastoid Cell Lines for Induced Pluripotent Stem Cell Generation. Stem Cells Int. 2016; 2349261.

Larson VA, Mironova Y, Vanderpool KG, Waisman A, Rash JE, Agarwal A, Bergles DE. Oligodendrocytes control potassium accumulation in white matter and seizure susceptibility. eLife. 2018; 7:e34829.

Lek M, Karczewski KJ, Minikel EV, Samocha KE, Banks E, Fennell T et al. Exome Aggregation Consortium. Analysis of protein-coding genetic variation in 60,706 humans. Nature 2016; 18:536(7616):285-91.

Lenzen KP, Heils A, Lorenz S, Hempelmann A, Ho¨ fels S, Lohoff FW, Schmitz B, Sander T. Supportive evidence for an allelic association of the human KCNJ10 potassium channel gene with idiopathic generalized epilepsy. Epilepsy Research 2005; 63:113–118.

Li H, Durbin R. Fast and accurate short read alignment with Burrows-Wheeler transform. Bioinformatics. 2009; 25(14):1754-60.

Lin DM, Goodman CS. Ectopic and increased expression of Fasciclin II alters motoneuron growth cone guidance. Neuron. 1994 Sep;13(3):507-23.

Littleton JT, Ganetzky B. Ion channels and synaptic organization: analysis of the Drosophila genome. Neuron. 2000 Apr;26(1):35-43

Lopatin AN, Makhina EN, Nichols CG. Potassium channel block by cytoplasmic polyamines as the mechanism of intrinsic rectification. Nature 1994; 24:372(6504):366-9.

Martin HC, Jones WD, McIntyre R, Sanchez-Andrade G, Sanderson M, Stephenson JD et al. A SINE Insertion in *ATP1B2* in Belgian Shepherd Dogs Affected by Spongy Degeneration with Cerebellar Ataxia (SDCA2). G3 (Bethesda). 2017;7(8):2729-2737.

McKenna A, Hanna M, Banks E, et al. The Genome Analysis Toolkit: a MapReduce framework for analyzing next-generation DNA sequencing data. Genome Res. 2010; 20(9):1297-303.

McLaren W, Gil L, Hunt SE, et al. The Ensembl Variant Effect Predictor. Genome Biol. 2016;17(1):122.

Melhem, M., Abu-Farha, M., Antony, D., Al Madhoun, A., Bacchelli, C., Alkayal, F., AlKhairi, I., John, S., Alomari, M., Beales, P. L., Alsmadi, O. Novel G6B gene variant causes familial autosomal recessive thrombocytopenia and anemia. Europ. J. Haemat 2016; 98: 218-227

Méndez-González MP, Kucheryavykh YV, Zayas-Santiago A, et al. Novel KCNJ10 Gene Variations Compromise Function of Inwardly Rectifying Potassium Channel 4.1. J Biol Chem. 2016; 291(14):7716-26.

Neusch C., Papadopoulos N., Muller M. et al. Lack of the Kir4.1 channel subunit abolishes K^+ buffering properties of astrocytes in the ventral respiratory group: impact on extracellular K^+ regulation. J. Neurophysiol. 2006; 95, 1843–1852.

Neusch C., Rozengurt N., Jacobs R. E., Lester H. A. and Kofuji P. Kir4.1 potassium channel subunit is crucial for oligodendrocyte development and in vivo myelination. J. Neurosci. 2001; 21, 5429–5438

Nwaobi S. E., Cuddapah V. A., Patterson K. C., Randolph A. C., Olsen M. L. The role of glial-specific Kir4.1 in normal and pathological states of the CNS. Acta Neuropathol. 2016; 132, 1–21.

Okonechnikov K, Conesa A, García-Alcalde F. Qualimap 2: advanced multi-sample quality control for high-throughput sequencing data. Bioinformatics. 2015; 32(2):292-4.

Olsen ML, Higashimori H, Campbell SL, Hablitz JJ, Sontheimer H. Functional expression of Kir4.1 channel in spinal cord astrocytes. Glia 2006; 53:516-28.

Olsen ML, Khakh BS, Skatchkov SN, Zhou M, Lee CJ, Rouach N. New Insights on Astrocyte Ion Channels: Critical for Homeostasis and Neuron-Glia Signaling. J Neurosci. 2015; 35(41):13827-35.

Paulais M, et al. Renal phenotype in mice lacking the Kir5.1 (Kcnj16) K+ channel subunit contrasts with that observed in SeSAME/EAST syndrome. Proc Natl Acad Sci USA. 2011;108(25):10361–10366.

Pessia M, Imbrici P, D'Adamo MC, Salvatore L, Tucker SJ. Differential pH sensitivity of Kir4.1 and Kir4.2 potassium channels and their modulation by heteropolymerisation with Kir5.1. J. Physiol. 2001; 532, 359–367.

Purcell S, Neale B, Todd-Brown K, et al. PLINK: a tool set for whole-genome association and population-based linkage analyses. Am J Hum Genet. 2007; 81(3):559-75.

Quinlan AR, Hall IM. BEDTools: a flexible suite of utilities for comparing genomic features. Bioinformatics. 2010; 26(6):841-2.

Reichold M, Zdebik AA, Lieberer E, et al. KCNJ10 gene mutations causing EAST syndrome (epilepsy, ataxia, sensorineural deafness, and tubulopathy) disrupt channel function. Proc Natl Acad Sci U S A. 2010; 107(32):14490-5.

Ryczko D, Grätsch S, Schläger L, Keuyalian A, Boukhatem Z, Garcia C, Auclair F, Büschges A, Dubuc R. Nigral Glutamatergic Neurons Control the Speed of Locomotion. J Neurosci. 2017; 4;37(40): 9759-9770.

Schirmer L, Möbius W, Zhao C, et al. Oligodendrocyte-encoded Kir4.1 function is required for axonal integrity. Elife. 2018;7: e36428.

Scholl UI, Choi M, Liu T, et al. Seizures, sensorineural deafness, ataxia, mental retardation, and electrolyte imbalance (SeSAME syndrome) caused by mutations in KCNJ10. Proc Natl Acad Sci U S A. 2009; 106(14):5842-7.

Schubert M, Lindgreen S, Orlando L. Adapter Removal v2: rapid adapter trimming, identification, and read merging. BMC Research Notes. 2016; 9:88.

Shawky RM, Elsayed SM, Zaki ME, et al. Consanguinity and its relevant to clinical genetics. Egyptian Journal of Medical Human Genetics. 2013; 14:157-64.

Sicca F, Ambrosini E, Marchese M, Sforna L, Servettini I, Valvo G, et al. Gain-of-function defects of astrocytic Kir4.1 channel in children with autism spectrum disorders and epilepsy. Scientific Reports 2016; 6:34325.

Sicca F, Imbrici P, D'Adamo MC, Moro F, Bonatti F, Brovedani P, et al. Autism with seizures and intellectual disability: possible causative role of gain-of-function of the inwardly-rectifying K+ channel Kir4.1. Neurobiology of Disease 2011; 43:239–247.

Simon JC, Dickinson MH. A new chamber for studying the behavior of *Drosophila*. PLoS One. 2010; 5(1): e8793.

Song F, Hong X, Cao J, et al. Kir4.1 channel in NG2-glia play a role in development, potassium signaling, and ischemia-related myelin loss. Commun Biol. 2018; 1:80.

Splinter K, Adams DR, Bacino CA, Bellen HJ, Bernstein JA, Cheatle-Jarvela AM, Eng CM, et al. Undiagnosed Diseases Network. Effect of Genetic Diagnosis on Patients with Previously Undiagnosed Disease. N Engl J Med. 2018; 29;379(22):2131-2139.

Srivastava R, Aslam M, Kalluri SR, et al. Potassium channel KIR4.1 as an immune target in multiple sclerosis. N Engl J Med. 2012; 367(2):115-23.

Suhas G, Husayn Ahmed P, Ravi Kumar Nadella, Ravi Prabhakar More, Manasa Seshadri, Biju Viswanath, Mahendra Rao, Sanjeev Jain, The ADBS consortium, Odity Mukherjee. Exome sequencing in families with severe mental illness identifies novel and rare variants in genes implicated in Mendelian neuropsychiatric syndromes. Psychiatry and Clinical Neurosciences 2018:

Sund KL, Zimmerman SL, Thomas C, Mitchell AL, Prada CE, Grote L, Bao L, Martin LJ, Smolarek TA. Regions of homozygosity identified by SNP microarray analysis aid in the diagnosis of autosomal recessive disease and incidentally detect parental blood relationships. Genet Med. 2013; 15(1):70-8.

Thompson DA, Feather S, Stanescu HC, et al. Altered electroretinograms in patients with KCNJ10 mutations and EAST syndrome. J Physiol. 2011; 589(Pt 7):1681-9.

Tong X, Ao Y, Faas GC, Nwaobi SE, Xu J, Haustein MD, et al. Astrocyte Kir4.1 ion channel deficit contributes to neuronal dysfunction in Huntington's disease model mice. Nat. Neurosci. 2014; 17, 694–703.

Van Poucke M, Stee K, Bhatti SF, et al. The novel homozygous KCNJ10 c.986T>C (p.(Leu329Pro)) variant is pathogenic for the SeSAME/EAST homologue in Malinois dogs. Eur J Hum Genet. 2016; 25(2):222-226.

Vaser R, Adusumalli S, Leng SN, Sikic M, Ng PC. SIFT missense predictions for genomes. Nat Protoc. 2016; 11(1):1-9.

Villa C, Combi R. Potassium Channels and Human Epileptic Phenotypes: An Updated Overview. Front Cell Neurosci. 2016; 10:81.

Wang K, Li M, Hakonarson H. ANNOVAR: functional annotation of genetic variants from high-throughput sequencing data. Nucleic Acids Research 2010: 38(16): e164.

Wang NH, Chen SJ, Yang CF, Chen HW, Chuang HP, Lu YH, Chen CH, Wu JY, Niu DM,

Chen YT. Homozygosity Mapping and Whole-Genome Sequencing Links a Missense Mutation in POMGNT1 to Autosomal Recessive Retinitis Pigmentosa. Invest Ophthalmol Vis Sci. 2016;57(8):3601-9.

Williams DM, Lopes CM, Rosenhouse-Dantsker A, et al. Molecular basis of decreased Kir4.1 function in SeSAME/EAST syndrome. J Am Soc Nephrol. 2010; 21(12):2117-29.

Xue Y, Ren J, Gao X, Jin C, Wen L, Yao X. GPS 2.0, a tool to predict kinase-specific phosphorylation sites in hierarchy. Mol Cell Proteomics. 2008; 7(9):1598-608.

Figure legends

Figure 1. Clinical diagnosis of SeSAME family members.
(A) Genogram of family with SeSAME syndrome with no electrolyte imbalance. The generations are marked in roman letters (I to V) and individuals in each generation are given running numbers. (B) All affected siblings showed dysmorphic facial features. (C) T2W image of IV.2 showing enlarged and bilateral basal ganglia (blue arrows) (D) T1 MPRAGE of IV.2 showing bilateral cerebellar atrophy (orange arrows) (E) EEG of V.1 showing generalized sharp and slow wave discharges predominantly in Fronto Central region (F) EEG of V.2 showing generalized poly spike discharges predominantly in Fronto-Temporal region. (G) Hierarchical clustering of 23 biochemical readouts from whole blood samples.

Figure 2. Identification of novel mutation in *KCNJ10* by homozygosity mapping and whole exome analysis of SeSAME family members.
(A) WES analysis pipeline and variant prioritization methods. (B) Principle component analysis (PCA) of exome-wide F-statistics explains for an overall variance of ~49% (PC1) between the SeSAME family members (purple ellipse) and healthy population controls (blue ellipse). The

dot-dash lines in the plot represents the 95% confidence ellipse (C) The zygosity of the *KCNJ10*^{T290A} variant was validated in all the six affected (HOM) and the four unaffected individuals (HET) within the pedigree. (D) A schematic reconstruction of Kir4.1 with the T290A variant (purple) mapped in the cytoplasmic C-terminal domain, along with other deleterious variants identified from previous studies. (E) Multiple sequence alignment (MSA) of the Kir4.1 protein sequence across species reveals the evolutionary conservation of T290A in VEST domain.

Figure 3. Novel Kir4.1^{T290A} mutation affects channel localization and function in patient-derived LCLs

(A) Projected *Z*-stacks of six LCLs showing the distribution of Kir4.1 in green, phalloidin to label F-actin in red and DAPI to label nucleus in blue. Scale bar, 10μm. (B) Quantitative measurement of cytoplasmic and nuclear punctae normalized against the cytoplasmic space (as measured by F-actin distribution) and nuclear space (as measured by DAPI distribution) in *Z*-stacks. (C) Anti-hKir4.1 western of six LCLs showing the distribution of both monomeric and multimeric forms of the protein. Arrow indicates the expression of Kir4.1 protein against beta-actin loading control (blot insert at the bottom). -/+ and -/- indicates the nature of zygosity of unaffected parents and affected individuals. (D) Densitometric plots representing the relative expression Kir4.1 protein from three independent western experiments is represented as mean±SEM. Data analyzed using ANOVA. (E) Whole-cell currents measured from healthy wild type controls and two unaffected parental controls in response to voltage step protocol from -120 to 40mV in presence and absence of 110μM barium. Cells were clamped at *Vm*, equal to resting *Vm (Vh=Vm)*. Histogram shows the subtraction of currents obtained with barium from whole-cell currents, which served as internal control for each experiment. Barium sensitive current shows the contribution of Kir channels to whole-cell currents in each LCLs. Data analysed by *k* independent Kruskal-Wallis test with Bonferroni correction and represented as ±S.E. (F) Average membrane potential of LCLs from healthy control (wild type), two unaffected parents (III.11 and III. 12) and four affected (IV.2 to IV.4). Data analyzed using *k* independent group one-way ANOVA test with Turkey-Kramer post hoc tests. (G) whole-cell patch clamp recordings in response to voltage-steps from -120 to 40mV in 10mV steps, from a holding potential of -30mV. Representative currents traces from respective LCLs. (H) Current-voltage relationship is summarized within -120 to 40mV range. (I) Summary of inward currents discharges measured in response to induced K^+ steps from 5-20 mM extracellular K^+. For improved Kir specificity, Kir current discharges measured with and without barium. Data analysed using *k* independent group one-way ANOVA test with Turkey-Kramer post hoc tests. Error bars represent ±S.E. ** represents $p<0.001$.

Figure 4. Generation and molecular characterization of *irk2* mutants

(A) Amino acid sequence alignment of *Drosophila* Irk2 and human Kir4.1. Identical amino acid residues are marked in white and black in grey background. Relative position of human Kir4.1 domain organization is marked in the alignment. The variant identified in this study is marked by *. (B) Genomic organization of *Drosophila irk2* locus and position of P element G8696. The regions deleted by P-element excision events are marked here. (C) RT-PCR analysis of cDNA extracted from fly heads of wild-type (WT), homozygous and heterozygous combinations of *irk2*^{e118} and *irk2*^{e91b} mutants using primers specific for irk2 coding region. cDNA derived from homozygous *irk2*^{e118} embryos were used for RT-PCR analysis since they are embryonic lethal.

Expression of neighboring gene (CG10177) and housekeeping gene RpL32 were used as internal control. (D) Survival percentage was evaluated for *irk2* mutants compared with wild-type controls, heterozygous irk2 mutants and heteroallelic combinations of *irk2* mutants. (E) Neuronal rescue experiments were performed with C155-G4 with UAS derivatives expressing both wild type and mutant forms of human Kir4.1 and *Drosophila* Irk2 proteins. Survival percentage was assayed for all above mentioned combinations both in wild-type and *irk2* mutant background (heteroallelic $irk2^{e118}/irk2^{e91b}$ combination referred as *irk2* mutant*).*

Figure 5. Kir4.1^{T290A} variant fail to ameliorate larval locomotion defects observed in *irk2* mutants

(A) Automatic traces of larval locomotor patterns generated for various genotypes. (B) Quantification of average speed, current length against mean length and peristaltic contractions for various genotypes tested here. Data analyzed by one-way ANOVA test with Turkey-Kramer post hoc tests ($p<0.005$ for all comparisons with their respective *irk2* mutant alone control). Error bars represent $\pm$S.E. ** represents $p<0.001$.

Figure 6. Locomotion impairment in *irk2* mutant adults

(A) Schematic of vertical climbing assay (Aggarwal et al 2018). (B) Average time spent by flies to complete one climb was higher in *irk* mutants as compared to the controls. (C) Average speed of the flies was lower for *irk* mutants as compared to controls. (B') and (C') represent track duration and average speed of the flies with respect to per unit time spent in the assay. The track duration and average speed of mutants at initial timepoints do not differ significantly from other timepoints, indicating no fatigue or metabolic defect (two-way repeated measures ANOVA, post-hoc Sidak's multiple comparisons). (D) Schematic of flyBowl setup (Simon and Dickinson, 2010). (E) Average speed of flies in the flyBowl assay in overall 15 minutes for *irk* mutant is significantly lower than controls. (E') time series analysis of average speed of flies shows significant decrease in speeds of *irk* mutants wrt controls post 6th minute into the assay ($p<0.01$ for all timepoints, two-way repeated measures ANOVA, post-hoc Sidak's multiple comparisons, $n>35$).

Figure 7. Age dependent degeneration of adult dopaminergic neurons in *irk2* mutants

(A) Graphical representation of anterior (left) and posterior (right) brain regions to show the TH-Gal4 labeled DA neuronal clusters. ML represents mid line (B) MIP of Z-stacks of TH>mCD8::GFP expressing adult brain stained with anti-nc82 and anti-GFP to label dopaminergic neurons in anterior and posterior regions of 3d and 30d old flies. Scale bar, 5µm (C) Quantification of number of DA neurons per brain hemisphere between wild type (n=13 and n=17) and *irk2* mutant (n=14; n=21) of 3d and 30d old flies. ns represents not significance and ** represents $p<0.001$.

Figure 1

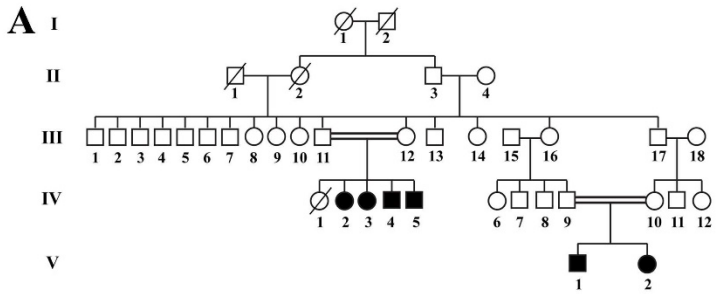

B

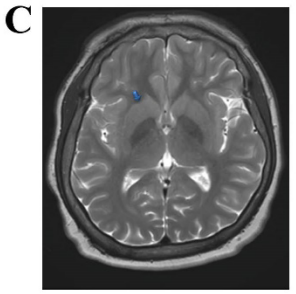

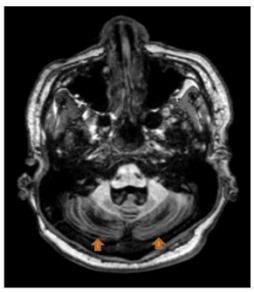

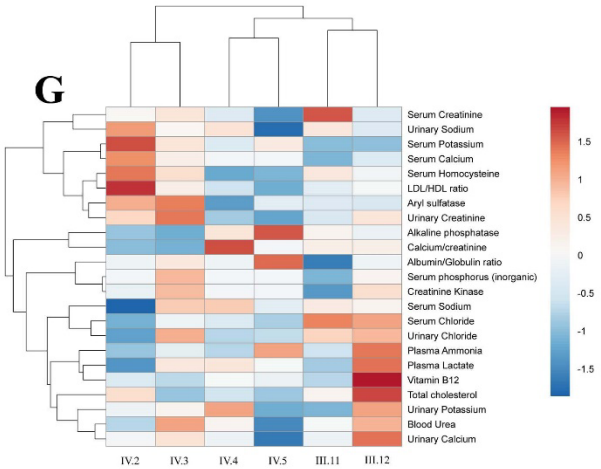

Figure 2

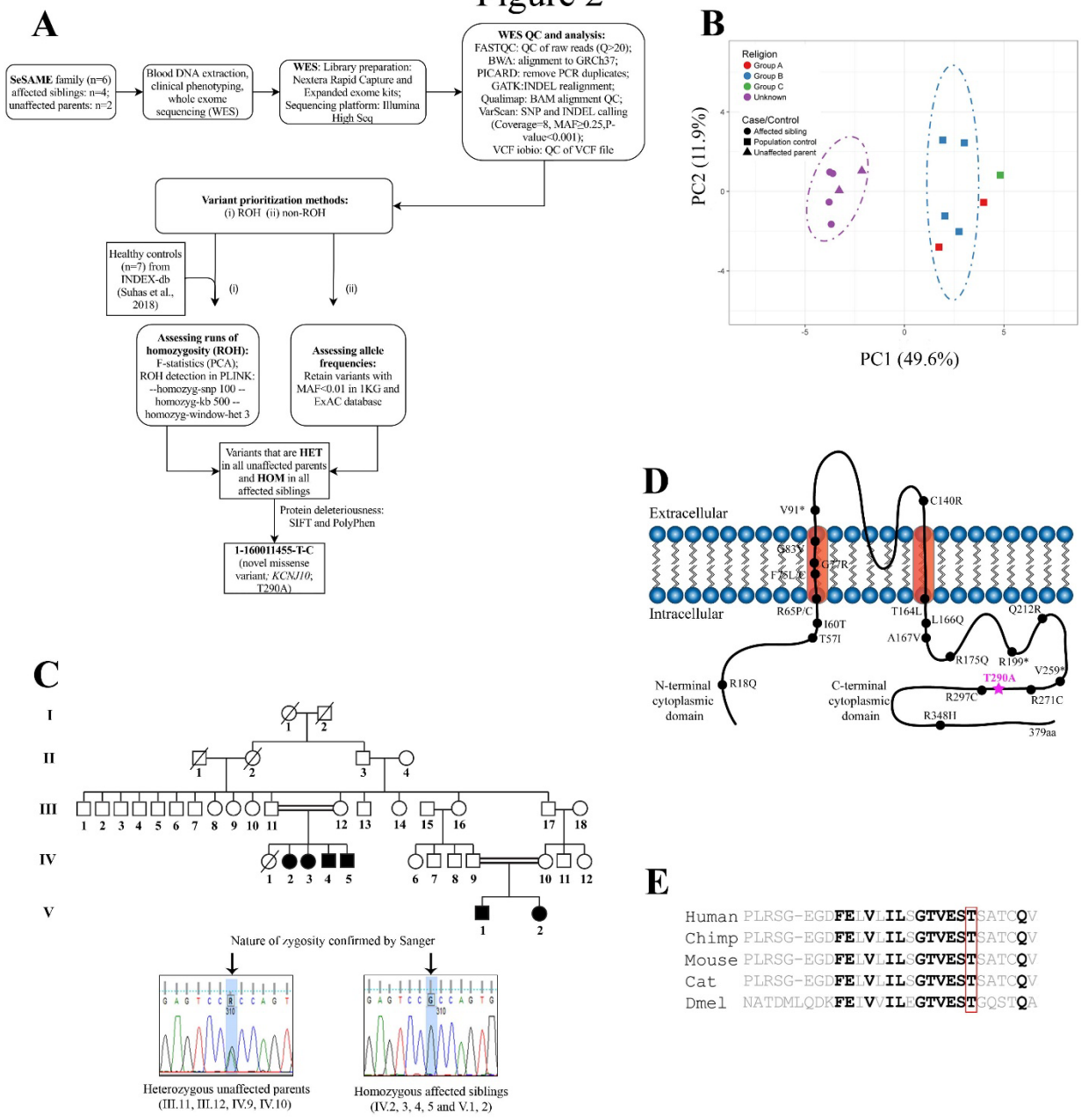

Figure 3

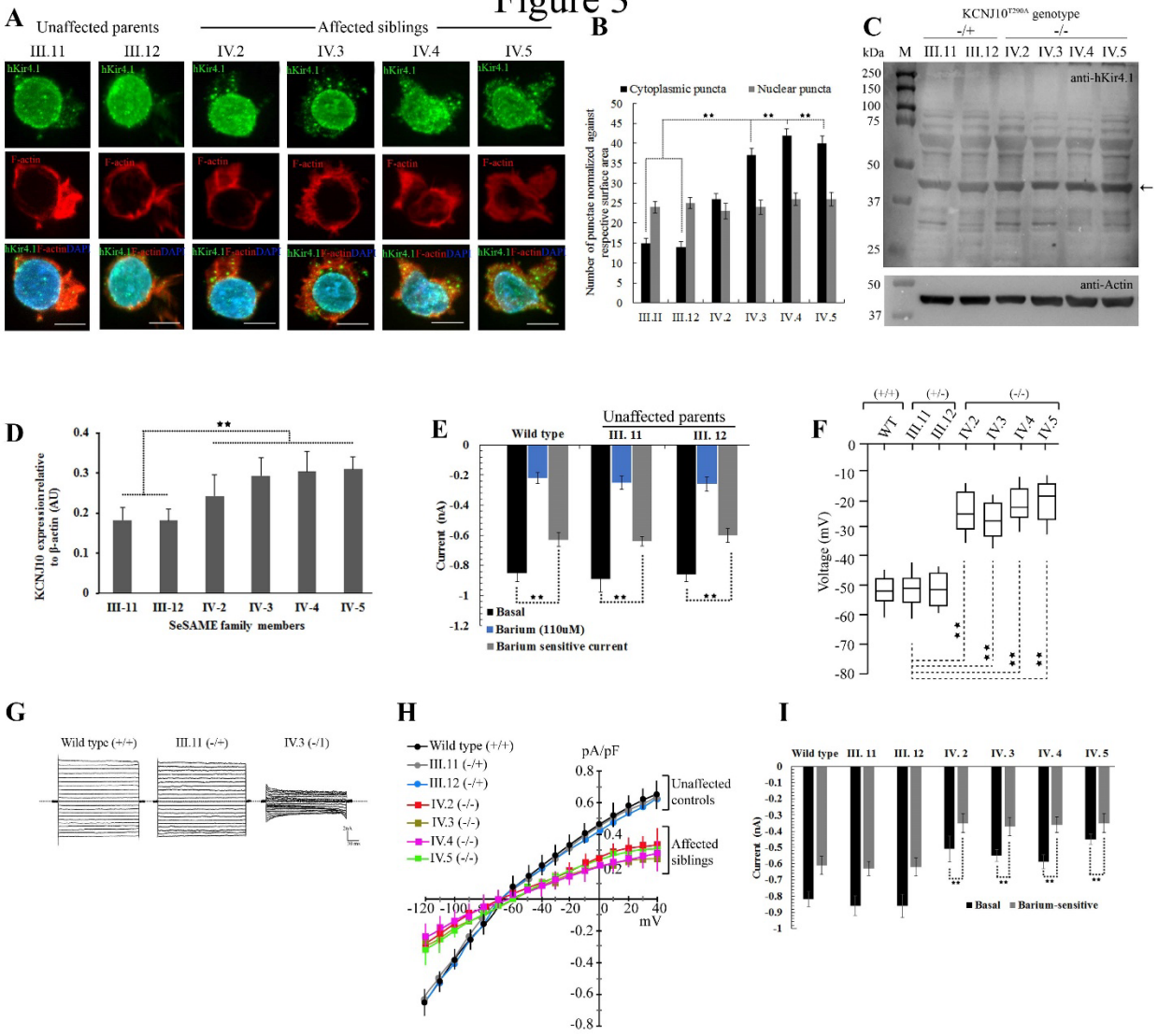

Figure 4

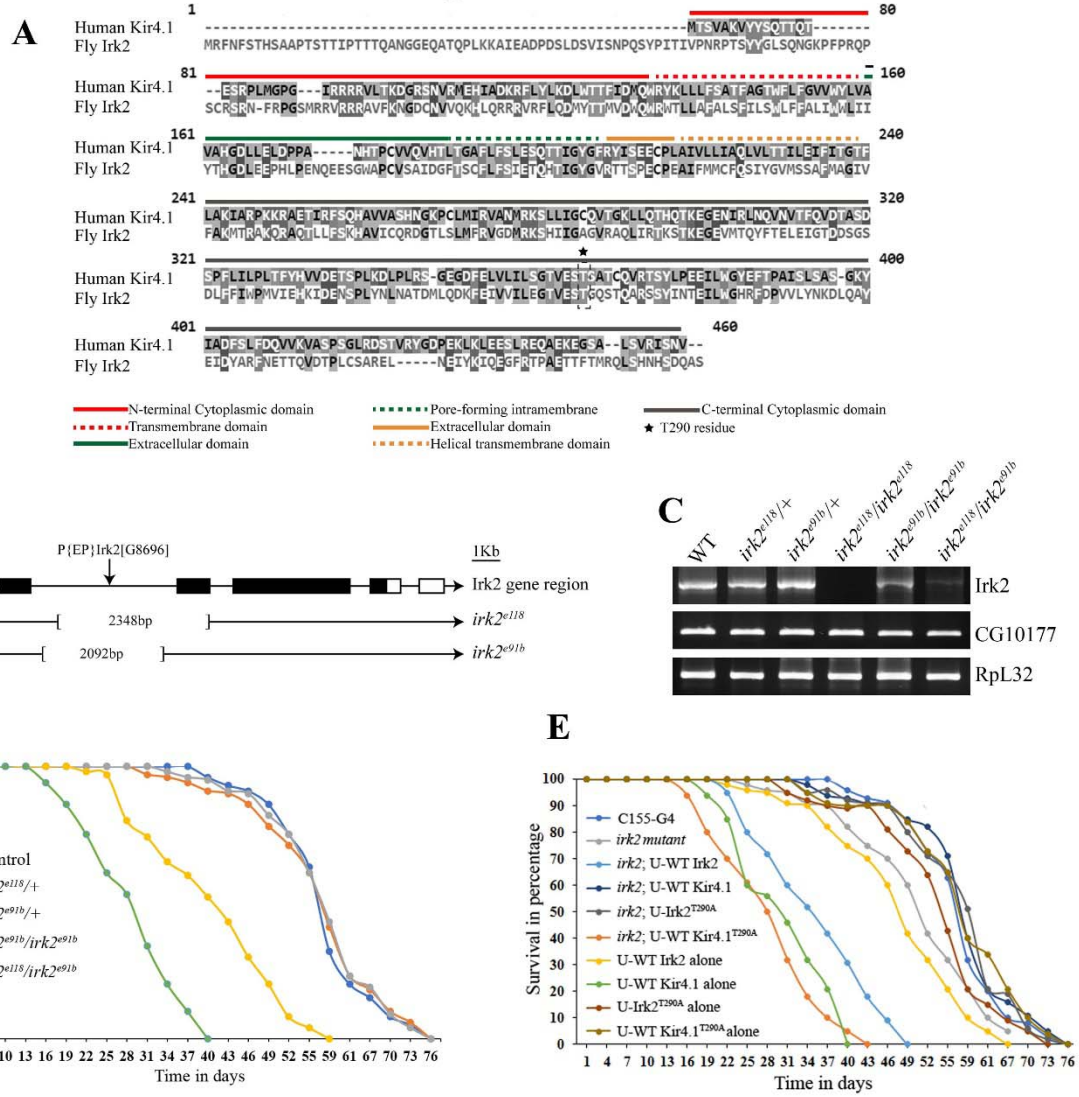

Figure 5

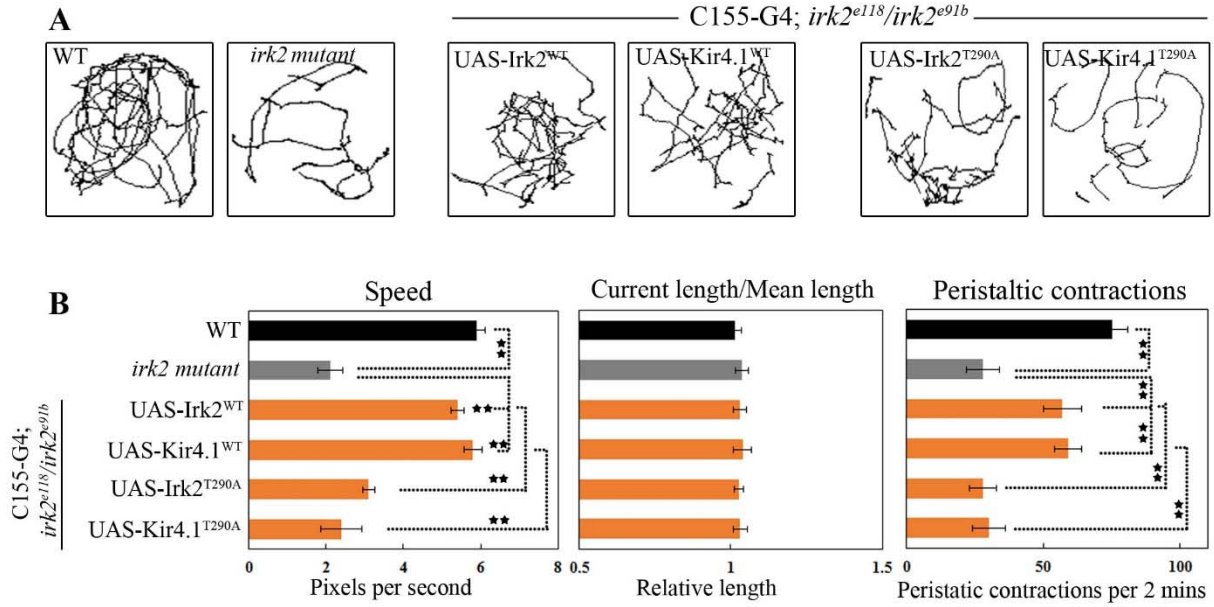

Figure 6

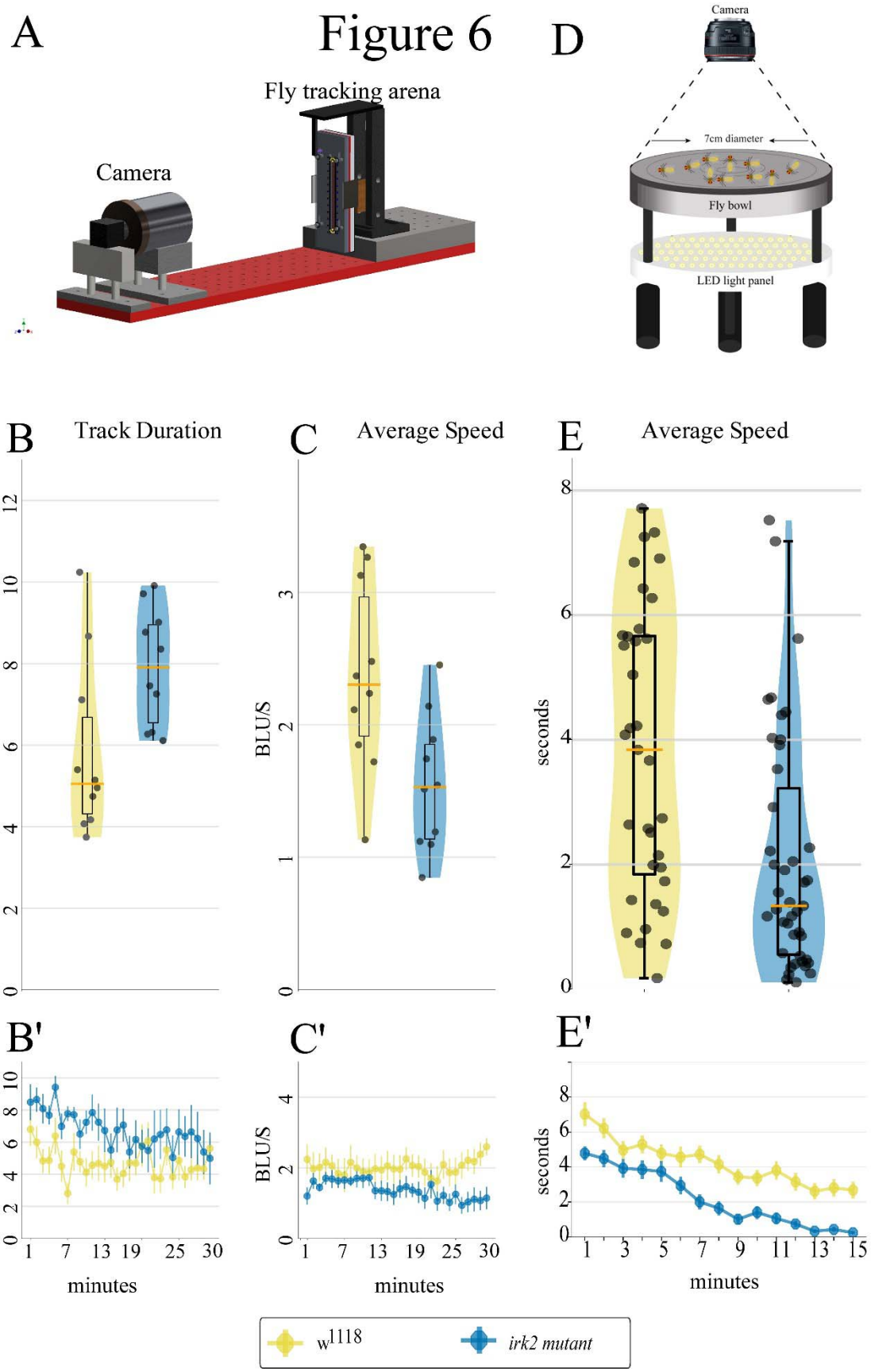

Figure 7

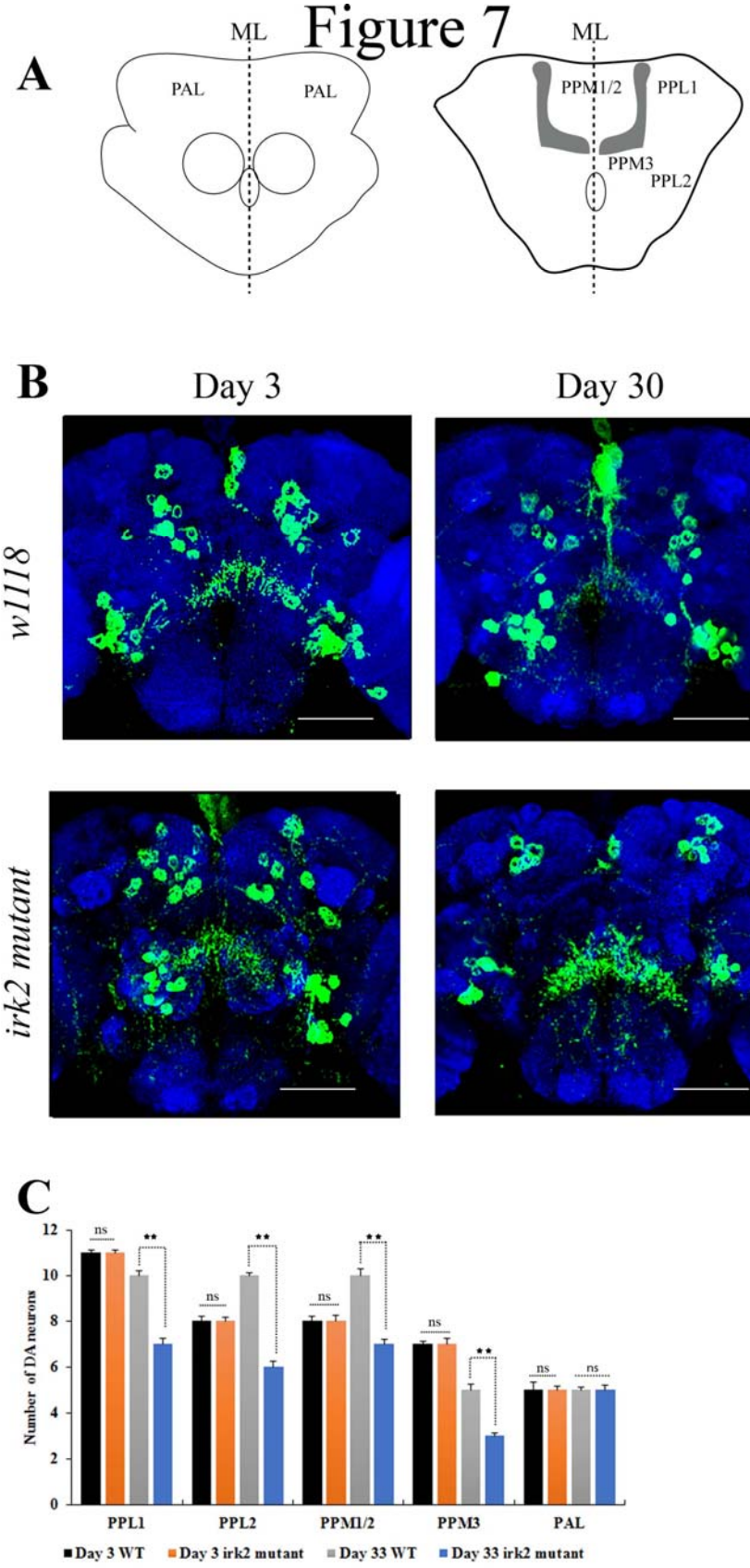

Table 1: Clinical information of the affected individuals in the pedigree

Clinical Information						
Features	**IV.2**	**IV.3**	**IV.4**	**IV.5**	**V.1**	**V.1**
Age	30	28	25	22	12	9
Gender	Female	Female	Male	Male	Male	Female
Developmental delay	++	++	++	++	++	++
Seizures	GTCS	GTCS	GTCS	GTCS	GTCS	GTCS
Ataxia	++	++	++	++	++	++
Nystagmus	Upgaze nystagmus	No	No	Horizontal gaze evoked	No	No
Incoordination	++	++	++	++	++	++
Muscle tone	Increased (spastic type)	Increased (spastic type)	Increased (spastic type)	Increased (spastic type)	Increased (spastic type)	Increased (spastic type)
DTRs	Exaggerated	Exaggerated	Exaggerated	Exaggerated	Exaggerated	Exaggerated
Plantar	Extensor	Extensor	Extensor	Extensor	Extensor	Extensor
Irritability	+	+	+	+	+	+
Stereotypes	-	-	+	-	+	-
Psychosis	+	-	-	-	-	-
Hyperactivity	-	-	+	-	+	+
Speech	Dysarthric (scanning+spastic)	Dysarthric (scanning+spastic)	Dysarthric (scanning+spastic)	Dysarthric (scanning+spastic)	No speech	No speech
Gait	Unable to walk	Unable to walk	Unable to walk	Unable to walk	Walks with support	Walks with support
Audiometry	Mild SNHL	Mild SNHL	Severe SNHL	Severe SNHL	Moderate SNHL	Moderate SNHL
IQ	Not Done	Not Done	Not Done	Not Done	Profound mental retardation*	Profound mental retardation*

* IQ is measured using Vineland Social Maturity Scale (VSMS) and found to be <20

Table 2. $ROH_{affected}$

Chr	Start	End
1	149726239	152185823
1	152883608	161561287
12	115109694	125324197
5	137206560	143131673
8	15398151	31024638

Supplementary Material

Supplementary Figure 1: Karyotypic and STR validation of six LCLs
(A) Metaphase chromosomal spreads of six LCLs.

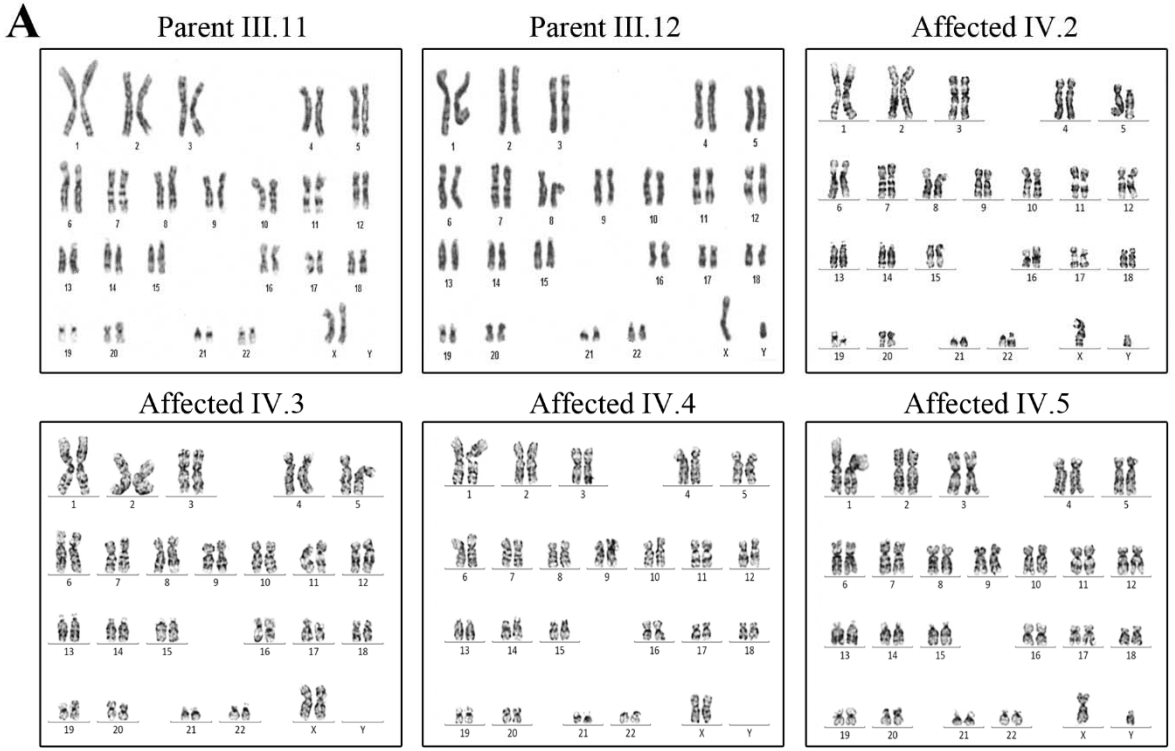

Supplementary Figure 2 PCA plot explaining the intra-familial levels of homozygosity between affected and un-affected members

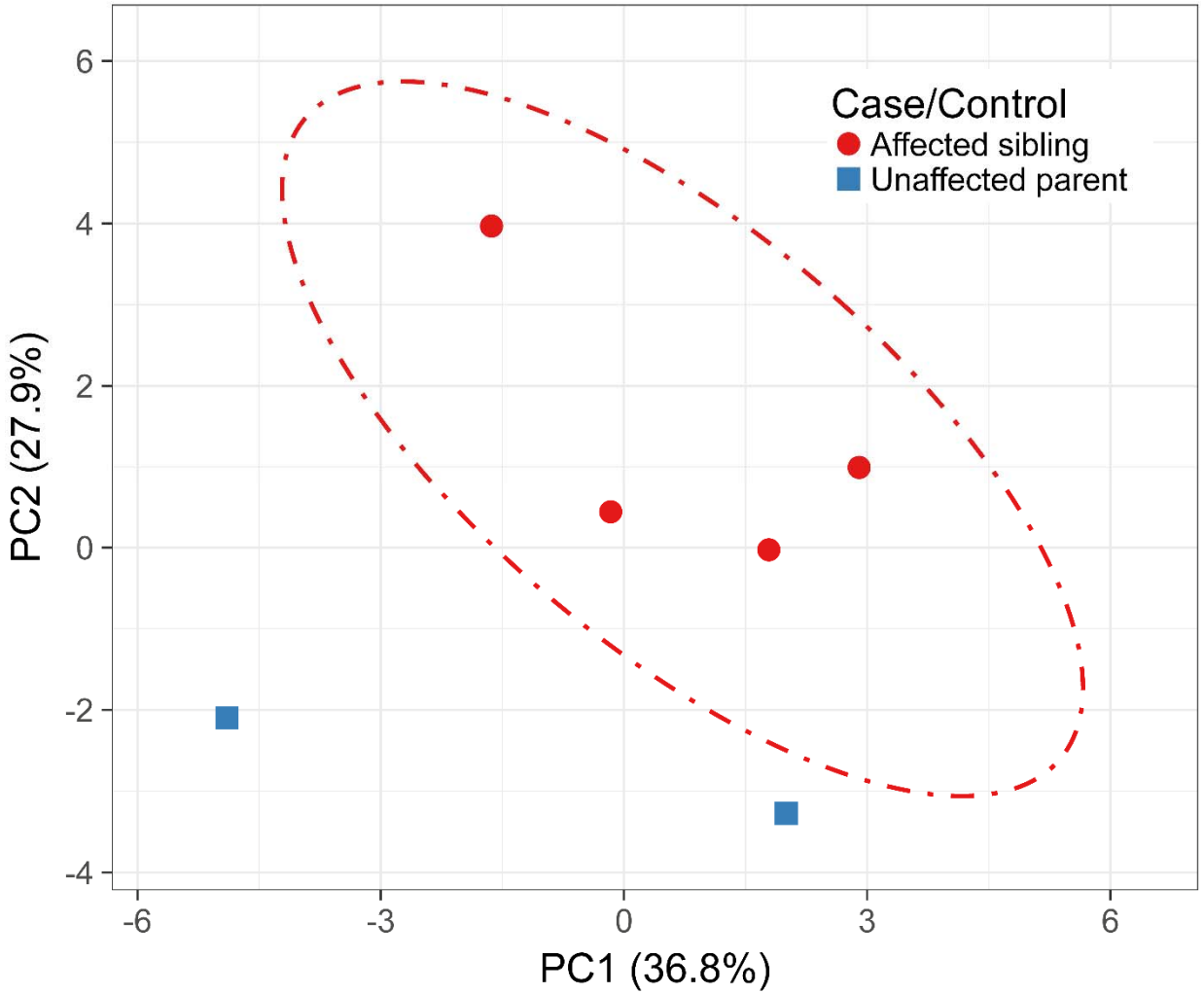

Supplementary Table 1: Biochemical investigations of all affected individuals in the SeSAME family

Biochemical investigation of affected siblings in SeSAME family							
Investigation	**Reference values**	**IV.1**	**IV.2**	**IV.3**	**IV.4**	**V.1**	**V.1**
Serum Sodium	136-146 mmol/L	137.4	137.3	136	137.7	137.7	137
Serum Potassium	3.5-5.1 mmol/L	3.68	3.69	4.23	3.98	3.81	3.95
Serum Chloride	101-109 mmol/L	104	103.5	98.5	100.9	100.2	99.2
Serum Calcium	8.8-10.6 mmol/L	9.14	9.45	10.2	9.73	Not done	Not done
Serum phosphorus (inorganic)	2.5-4.5 mmol/L	2.9	3.2	Not done	3.4	Not done	Not done
Plasma Ammonia	11-51 umol/L	38	50	36	40	37	48
Plasma Lactate	4.5-20 mg/dL	12.6	22	10.3	17.6	17.8	16.2
Creatinine Kinase	<171 U/L	58	90	78	96	Not done	Not done
Serum Bilirubin	0.3-1.2 mg/dL	0.35	0.23	0.35	0.35	0.27	0.28
SGOT	8-35 U/L	24.4	27.8	25.3	30.7	25	25
SGPT	7-35 U/L	18.1	19.7	21	22.7	17	13
Alkaline phosphatase	30-120 U/L	151	142	123	117	158	188
Serum Albumin	3.5 - 5.2 g/dL	3.59	3.93	4.39	4.14	3.76	4.11
Serum Globulin	2.5-5.6 g/dL	4.2	3.6	3.9	-	3.4	3.1

Albumin/Globulin ratio	1.2-2.5	0.9	1.1	1.1	1.16	-	1.3
Total Protein	6.6-8.3 g/dL	7.74	7.56	8.27	7.68	7.1	7.2
Blood Urea	17-43 mg/ dL	21.4	25.4	18.3	26	22	15
Serum Creatinine	0.66-1.09 mg/ dL	0.82	0.62	0.66	0.7	0.62	0.51
Total cholesterol	<200 mg/ dL	195	241	207	162	173	163
HDL cholesterol	40-60 mg/ dL	56.2	65.1	38.8	41.6	55.5	75
LDL cholesterol	<100 mg/ dL	121	157	156	108	104	85
Serum Triglycerides	<150 mg/ dL	88	93	63	61	66	62.7
VLDL	5-30 mg/ dL	18	19	13	12	13	15
Aryl sulfatase	35-130 nmol/4hrs/ml	87	86	104	108	75	88
Vitamin B12	180-914 pg/ml	166	277	180	168	197	189
Serum Homocysteine	<15 umol/L	16	14	21	17	8.5	9.0
Urinary Sodium	10-250 mmol/L	170	141	202	157	174	85
Urinary Potassium	1-100 mmol/L	23.74	61.69	40.92	45.77	62.35	22.4
Urinary Chloride	10-250 mmol/L	180.9	195.5	45.7	201.2	81.3	86.3
Urinary Calcium	0.6-30 mg/ dL	3.5	6.1	3.7	4.5	3.5	1.0
Urinary Creatinine	0.31-367 mg/ dL	118.8	208.5	236.6	311.5	77.2	37.5
Calcium/creatinine	<0.14	0.0294	0.0292	0.0156	0.0144	0.0453	0.0266
Screening for Inborn Errors of Metabolism	-	Negative	Negative	Negative	Negative	Negative	Negative
Urine screening for abnormal metabolites	-	Negative	Negative	Negative	Negative	Negative	Negative

Supplementary Table 2: ROH (n=56) (either overlapping or unique) detected within the exomes of all cases and controls. No ROH detected in the populations controls 7, 8 and 9.

Supplementary Table 3: List of variants (n=78) within $ROH_{affected}$ that were HET in all of the unaffected parents and HOM in all of the affected siblings. (0/1 = HET; 1/1 = HOM)

Supplementary Table 4: Variants (n=7) shortlisted based on assessing the allele frequencies (MAF<0.01) in 1KG_all and ExAC_all. The below variants are the only those which were HET in all unaffected parents and HOM in all affected siblings.

Supplementary Video 1: Live imaging of a single adult wild type and *irk2* mutant fly climbing in vertical arena. Note the reduced speed and distance travelled by *irk2* mutant compared with wild type.

Supplementary Video 2: Live imaging of wild type and *irk2* mutant flies in flyBowl assay